Title	Graphene oxide modulates inter-particle interactions in 3D printable soft nanocomposite hydrogels restoring magnetic hyperthermia responses
Authors(s)	Rani Aluri, Esther, Gannon, Edward, Singh, Krutika, Kolagatla, Srikanth, Kowiorski, Krystian, Shingte, Sameer, McKiernan, Eoin, Moloney, Cara, McGarry, Katie, Jowett, Liam, Rodriguez, Brian J., Brougham, Dermot F., Wychowaniec, Jacek K.
Publication date	2022-04-01
Publication information	Rani Aluri, Esther, Edward Gannon, Krutika Singh, Srikanth Kolagatla, Krystian Kowiorski, Sameer Shingte, Eoin McKiernan, et al. “Graphene Oxide Modulates Inter-Particle Interactions in 3D Printable Soft Nanocomposite Hydrogels Restoring Magnetic Hyperthermia Responses.” Elsevier, April 1, 2022. https://doi.org/10.1016/j.jcis.2021.12.048.
Publisher	Elsevier
Item record/more information	http://hdl.handle.net/10197/12738
Publisher's statement	This is the author’s version of a work that was accepted for publication in Journal of Colloid and Interface Science. Changes resulting from the publishing process, such as peer review, editing, corrections, structural formatting, and other quality control mechanisms may not be reflected in this document. Changes may have been made to this work since it was submitted for publication. A definitive version was subsequently published in Journal of Colloid and Interface Science (611, (2021)) https://doi.org/10.1016/j.jcis.2021.12.048
Publisher's version (DOI)	10.1016/j.jcis.2021.12.048

Graphene oxide modulates inter-particle interactions in 3D printable soft nanocomposite hydrogels restoring magnetic hyperthermia responses

Esther Rani Aluri[1], Edward Gannon[1], Krutika Singh[1], Srikanth Kolagatla[2,3], Krystian Kowiorski[4], Sameer Shingte[1], Eoin M^c^Kiernan[1], Cara Moloney[1], Katie M^c^Garry[1], Liam Jowett[1], Brian J. Rodriguez[2,3], Dermot F. Brougham[1,*], Jacek K. Wychowaniec[1,*,◊]

[1]School of Chemistry, University College Dublin, Belfield, Dublin 4, Ireland

[2]Conway Institute of Biomolecular and Biomedical Research, University College Dublin, Belfield, Dublin 4, Ireland

[3]School of Physics, University College Dublin, Belfield, Dublin 4, Ireland

[4]Łukasiewicz Research Network - Institute of Microelectronics and Photonics, Research group - Functional Materials, Lotników 32/46, 02-668 Warsaw

◊ Current address:

AO Research Institute Davos, Clavadelerstrasse 8, 7270, Davos, Switzerland

e-mail: jacek.wychowaniec@aofoundation.org

♦ These authors contributed equally to this work.

* Corresponding authors:

J.K.W. Phone: (+41)0779238956;

e-mails: jacek.wychowaniec@ucd.ie; jacek.wychowaniec@aofoundation.org

D.F.B. Phone: (+353)017162077;

e-mail: dermot.brougham@ucd.ie

Table of Content Graphics:

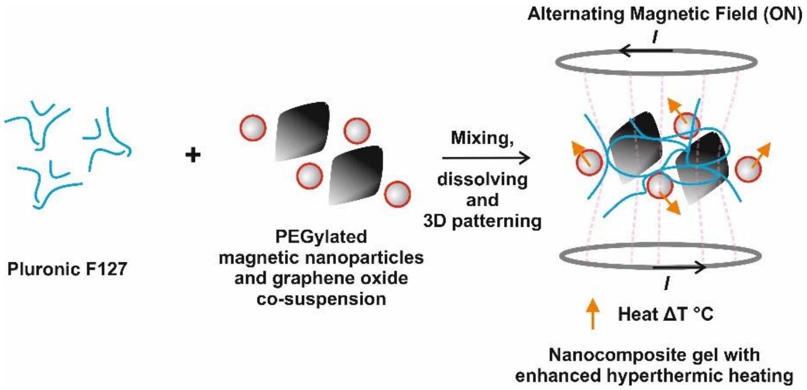

Abstract

Hydrogels loaded with magnetic iron oxide nanoparticles that can be patterned and which controllably induce hyperthermic responses on AC-field stimulation are of interest as functional components of next-generation biomaterials. Formation of the nanocomposite hydrogels is known to eliminate any Brownian contribution to hyperthermic response (reducing stimulated heating) while the Néel contribution can also be suppressed by inter-particle dipolar interactions arising from aggregation induced before or during gelation. We describe the ability of graphene oxide (GO) flakes to restore the hyperthermic efficiency of soft printable hydrogels formed using Pluronics F127 and PEGylated magnetic nanoflowers. Here, by varying the amount of GO in mixed nanocomposite suspensions and gels, we demonstrate GO-content dependent recovery of hyperthemic response in gels. This is due to progressively reduced inter-nanoflower interactions mediated by GO, which largely restore the dispersed-state Néel contribution to heating. We suggest that preferential association of GO with the hydrophobic F127 blocks increases the preponderance of cohesive interactions between the hydrophilic blocks and the PEGylated nanoflowers, promoting dispersion of the latter. Finally we demonstrate extrusion-based 3D printing with excellent print fidelity of the magnetically-responsive nanocomposites, for which the inclusion of GO provides significant improvement in the spatially-localized open-coil heating response, rendering the prints viable components for future cell stimulation and delivery applications.

Keywords: Magnetic nanoflowers; Magnetic hydrogels; Graphene oxide; Magnetic hyperthermia; 3D printing

1. Introduction

Magnetic nanoparticles (MNPs) are currently used and are under development for multiple biomedical applications including cancer treatment, as delivery/release agents in vitro and in vivo and as contrast agents for magnetic resonance imaging, due to their controlled responses to applied magnetic fields which are strongly dependent on the particles dispersion state [1-5]. Graphene and graphene oxide (GO) are being widely explored for liquid crystal [6] and electronics applications [7], and as composites [8] often for tissue engineering as they can provide functional responses and can modulate the aggregation state of other nanocomposite components [9, 10], providing means to control the final physical (*e.g.* mechanical or thermal) properties. Materials studied in this regard include hydrogels [11-14]. Hence the intrinsic functional potential and controlled component interactions arising from including, for instance, MNPs and GO flakes as nanocomposite fillers within polymer matrices offers opportunities for designing responsive systems. Mourdikoudis *et al.* recently reviewed synthesis, physicochemical properties, and applications of magnetic nanocomposites, noting the use of graphene and GO as support surfaces for immobilizing MNPs as an emerging route to functional nanocomposites [15].

Amongst possible matrix formers, pluronics, or poloxamers, are thermoresponsive tri-block co-polymers, composed of hydrophilic poly(ethylene) oxide (PEO) blocks flanking a more hydrophobic central poly(propylene) oxide (PPO) block, commonly used for stabilizing nanomaterials and forming soft hydrogels. The variation in hydrophobicity, which is block length-dependent, renders the materials thermoresponsive [16, 17]. Above a phase transition temperature well-defined micelles are observed with PPO blocks forming a hydrophobic core and PEO a hydrophilic shell [17-19], as a result gels are typically observed at room temperature for $\geq$ 21 w/v%, depending on molecular weight. Pluronics provide a tuneable ‘soft’ shear-thinning matrix with is usually injectable or printable at room temperature, with

Pluronic F127 (or F127, of average formula PEO_{101}-PPO_{56}-PEO_{101}, with the sol→gel transition at ~4 ^{o}C and excellent room-temperature shear-thinning) a particularly common choice.

GO, MNPs, and some combinations of these have been investigated as nano-fillers in F127 matrices with the focus of most studies on understanding the inter-particle interactions [20-24]. The addition of GO alone to F127 provided a responsive injectable hydrogel, capable of undergoing phase transition upon infrared (IR) irradiation or change of temperature or pH [21]. The encapsulated GO flakes were described as inducing changes in the polymer self-assembly due to stronger hydrophobic GO-PPO interactions, and with the hydrophilic poly(ethylene) oxide (PEO) chains extending into surrounding water [20, 21]. This reflects the consensus view as recently reviewed by Alegret *et al.* [25]. Other related reports focusing on biomedical application include Li *et al.* who described MNPs both physically [22] and chemically [23] linked to GO, encapsulated within an F127 coating to form hybrid micellar nanocomposite suspensions (nanogels) as carriers for pH-dependent doxorubicin delivery [22], and as magnetic resonance imaging-trackable Dox carriers [23]. Bulk hydrogels containing MNP-functionalized GO were also developed for combined again Dox release and hyperthermic therapy [26].

AC magnetic field heating of MNPs (hyperthermia) arises due to coupling of the particle moment with the applied field due to particle rotation (Brownian contribution) or moment re-orientation (Néel contribution). The hyperthermic efficiency can be quantified using the specific absorption rate (SAR) of AC-field energy, under quasi-adiabatic conditions, and is commonly used as a comparison between samples, SAR (W g^{-1}) is defined as;

$$\mathrm{SAR} = \frac{CV_s}{m_{\mathrm{Fe}}} \cdot \left[\frac{dT}{dt}\right]_{t=0} \qquad (1)$$

where C is the volumetric heat capacity of the medium (J mL^{-1} ^{o}C^{-1}), V_s the suspension volume (mL), m_{Fe} the mass of iron (g) obtained using flame atomic absorption spectroscopy and $\left[\frac{dT}{dt}\right]_{t=0}$ (^{o}C s^{-1}) defines an initial slope of the temperature-time plot usually extracted as the linear term from a polynomial fit, a commonly accepted approach [27], stemming from the presence of radiation and its fourth-power temperature dependence and the desire to weigh the linear part to the earliest (close to adiabatic) part of the response [28]. We used a fourth order polynomial, as is common practice [27], see Methods. Encapsulation of MNPs within hydrated networks and hydrogels suppresses any Brownian SAR contribution by constraining particle motion [29], while any Néel contribution can be reduced by inter-particle dipolar interactions due to aggregation induced before or during gelation [30].

We recently described nanocompositing of MNPs, in this case unmodified magnetic iron oxide nanoflowers (NFs), with F127 to form 3D-printable hydrogels that provided spatiotemporally-controlled temperature increase and associated dye release, on AC-field irradiation [24]. We found that the SAR value was indeed suppressed on gelation, although sufficient response was observed at high NF concentration (Fe 140 mg mL^{-1}) to demonstrate the principle. Our interpretation was that the Néel contribution, which is known to dominate over the Brownian for nanoflowers [31] was partially suppressed due to some aggregation. Higher SAR values are preferable as they allow for better control over the hyperthermic response (higher temperature jump realised in the applications format) and the use of lower particle concentration which may facilitate, for instance, UV-initiated crosslinking for downstream processing.

In this study we evaluated the possibility of improved nanocomposite hydrogels comprised of F127, NFs and GO. It was anticipated that planar GO flakes would mediate F127-induced NF aggregation, maintaining NF separation, and recovering the high hyperthermic potential of NFs. SAR values were screened for nanocomposite suspensions and gels of different composition, to elucidate the role of GO depending on the NF surface chemistry (unmodified or PEGylated). It was shown to be possible to recover most of the native SAR under certain conditions. Finally spatial patterning of the magnetic F127-GO nanocomposite hydrogels was demonstrated with significant improvement in hyperthermic response, as compared to GO-free equivalents, observed when using an open coil AC-field system suitable for cell culture or other biomedical applications.

2. Results and Discussion

2.1.Formation of nanocomposites

Magnetic iron oxide nanoflowers (NFs) were synthesized using a minor adaptation of the procedure developed by Hugounenq *et al.* [32]. A typical synthesis, see Methods, provides NF suspensions with a Fe yield of ~49%. The TEM size of 29 ± 3 nm (***Figure 1A***) obtained for NFs is similar to our previous report [24] and the low average hydrodynamic size of 37 nm and low polydispersity (PDI) of 0.17 obtained at pH 4 demonstrate full particle dispersion (***Figure 1A*** and ***E***). Suspensions of unmodified as-produced, or bare, NFs (here named BNFs) are not stable at physiological pH of 7 due to the absence of net surface charge (***Figure S1B***), as is most often required for biomedical applications and nanocompositing. Therefore polyethylene glycol (PEG) chains of 8000 Da were grafted to the NF surfaces, following the protocol described by Studart *et al.* [33] (***Figure 1B*** and ***S1A-C***), see Methods, forming PEGylated NF suspensions (named PNFs). PNFs are found to be 41 ± 4 nm in size (mean and standard deviation of measurements for 30 PNFs) from the amplitude modulation mode atomic force microscopy (AFM) height image (***Figure 1C***). The corresponding magnetic force microscopy (MFM) phase image recorded during lift-mode operation shows a phase shift associated with the resonance curve shift due to the long-range magnetic force gradient arising from PNFs (***Figure 1D***). Surface coating was evident from the increase of hydrodynamic size from *c*.37 nm at pH 4 for BNFs, to *c*.58 nm (again with low PDI of 0.18) for PNFs at neutral pH (***Figure 1E***), which is in the expected range given the graft chain length. Steric stabilization of PNFs is also confirmed by the close to neutral zeta potential (ζ_p) at pH 7, and by the broad pH range, from 6-10, over which the hydrodynamic size remains unchanged (***Figure S1C***). Full particle dispersion of these single-component suspensions is also evident from the hyperthermic properties, see below.

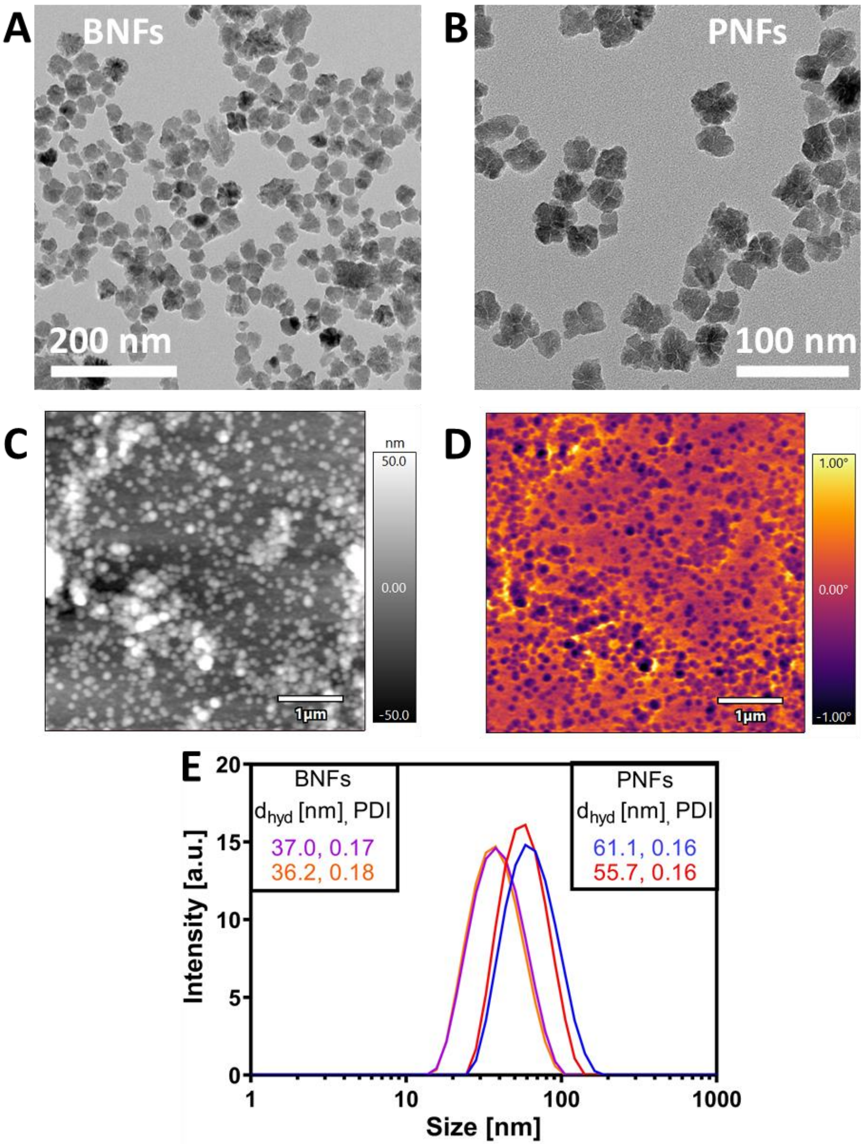

Figure 1. *Representative TEM images of;* ***(A)*** *bare magnetic nanoflowers (BNFs) at a 0.27 mg mL^{-1} Fe concentration with average size, d$_{TEM}$ 29 ± 3 nm (n≥100);* ***(B)*** *PEGylated nanoflowers (PNFs, with PEG MW 8000 Da) with d$_{TEM}$ 29 ± 2 nm (n≥100); Amplitude*

modulation mode height, ***(C)*** *and lift-mode (50 nm distance) magnetic force microscopy (MFM) phase,* d_{AFM} *41 ± 4 nm,* ***(D)*** *images of PNFs obtained using an MFM probe.* ***(E)*** *DLS intensity size distribution of two independently prepared representative batches of aqueous NF suspensions, with average* d_{hyd} *37 nm (PDI 0.18) and 58 nm (PDI 0.16) for sBNF (at pH 4) and sPNF (at pH 7), respectively.*

Graphene oxide was synthesized using a modified Hummers' method [34], see Methods. Here, we considered small GO flakes of size 240 ± 20 nm (a full characterization of the flakes is provided in Methods and shown in ***Figures S2*** and ***S3***). GO flakes are typically sterically- and charge-stabilized across pH values up to basic with ζ_p of -42 ± 3 mV at pH 7 (***Figure S3A***) [35].

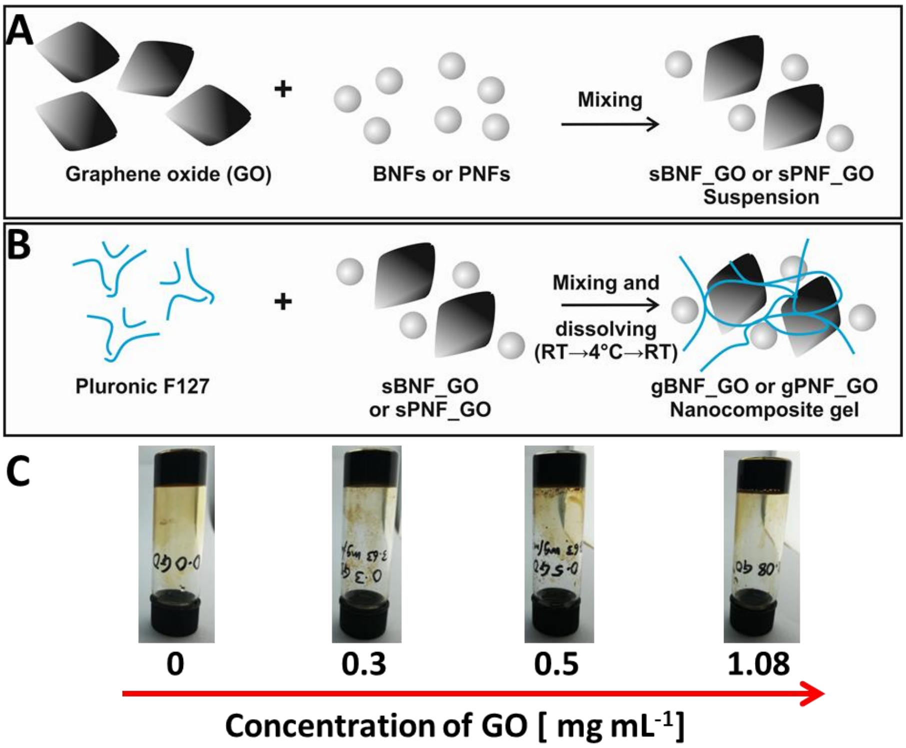

Scheme 1. *Schematic representation of;* ***(A)*** *formation of a NF GO mixed co-suspension (named sBNF_GO or sPNF_GO) and in this case presented as fully dispersed;* ***(B)*** *dissolution of Pluronic F127 polymers in sBNF_GO or sPNF_GO to form a (fully dispersed)*

nanocomposite gel, named throughout as gBNF_GO or gPNF_GO; ***(C)*** *Photographs of inverted vials of fabricated gPNF_GO as a function of GO concentration, at a concentration of Fe ~2.7 ± 0.3 mg mL^{-1}. Photographs were taken at room temperature following full fabrication cycle and were hydrogels upon inverted vial test.*

BNF, or PNF, and GO suspensions were mixed at the appropriate pH to ensure dispersion (***Scheme 1A***) and in different ratios, see Methods, to form stable co-suspensions (named sBNF_GO or sPNF_GO, see ***Table 1***). The sPNF_GO co-suspensions displayed homogeneity and stability at pH 7, indicating weak interactions between PNFs which at neutral pH have ζ_p close to zero (***Figure S1B***), and GO flakes which at neutral pH have ζ_p of -42±3 mV (***Figure S3A***). Increasing the amount of GO in the co-suspensions induced an apparent ζ_p decrease to close to that of the single-component GO suspension (***Figure 2A***), *i.e.* with increasing content flakes progressively dominate the charge profile. Similarly, at constant GO concentration of 0.5 mg mL^{-1}, as the Fe concentration was increased the ζ_p value increased progressively towards neutral (***Figure 2B***). Weak interactions are evident in TEM images, where the majority of PNFs are found around the edges of GO flakes (***Figure 2C-D***). Similarly, the PNFs were visible in the vicinity of GO flakes in AFM and MFM images, where MFM phase shift is again observed for PNFs (***Figure 2E-F***).

Table 1. *Sample naming convention.*

Sample names			
BNFs	B defines 'bare' nanoflowers without any ligand coating	**P**NFs	**P** defines PEGylated NFs.
sBNF or **s**PNF	s defines single component suspension	**g**BNF or **g**PNF	g defines nanocomposite hydrogel prepared at 40 w/v% F127
sBNF_GO or **s**PNF_GO or **g**BNF_GO or **g**PNF_GO	Defines two component suspension or gel	**s**BNF_0.5GO or **s**PNF_0.5GO or **g**BNF_0.5GO or **g**PNF_0.5GO	Defines sample at fixed GO concentration of 0.5 mg mL^{-1}

To form nanocomposite hydrogels F127 powder was dissolved in sBNF_GO or sPNF_GO (MNF-GO co-suspensions), at the appropriate concentrations, followed by gel-sol-gel re-fabrication by cycling from room temperature to 4^{o}C and back to room temperature. The resulting gels were stable and appeared homogeneous even after a single cycle (***Scheme 1B*** and ***1C***) and are named here as gBNF_GO or gPNF_GO (see ***Table 1***). SEM-EDX revealed similar distribution of Fe signal (~0.3 at%) across all gel samples, originally prepared at a Fe concentration of ~2.7 ± 0.3 mg mL^{-1} (***Figure S4***). These findings show that the nanocomposite gels are homogeneous as was further confirmed by hyperthermia measurements (next section). Finally, all electron micrographs show the porous structures expected for hydrogels (***Figure S4***). The magnetic properties, and in particular the AC-field hyperthermia responses, of the nanocomposite suspensions and gels are described below.

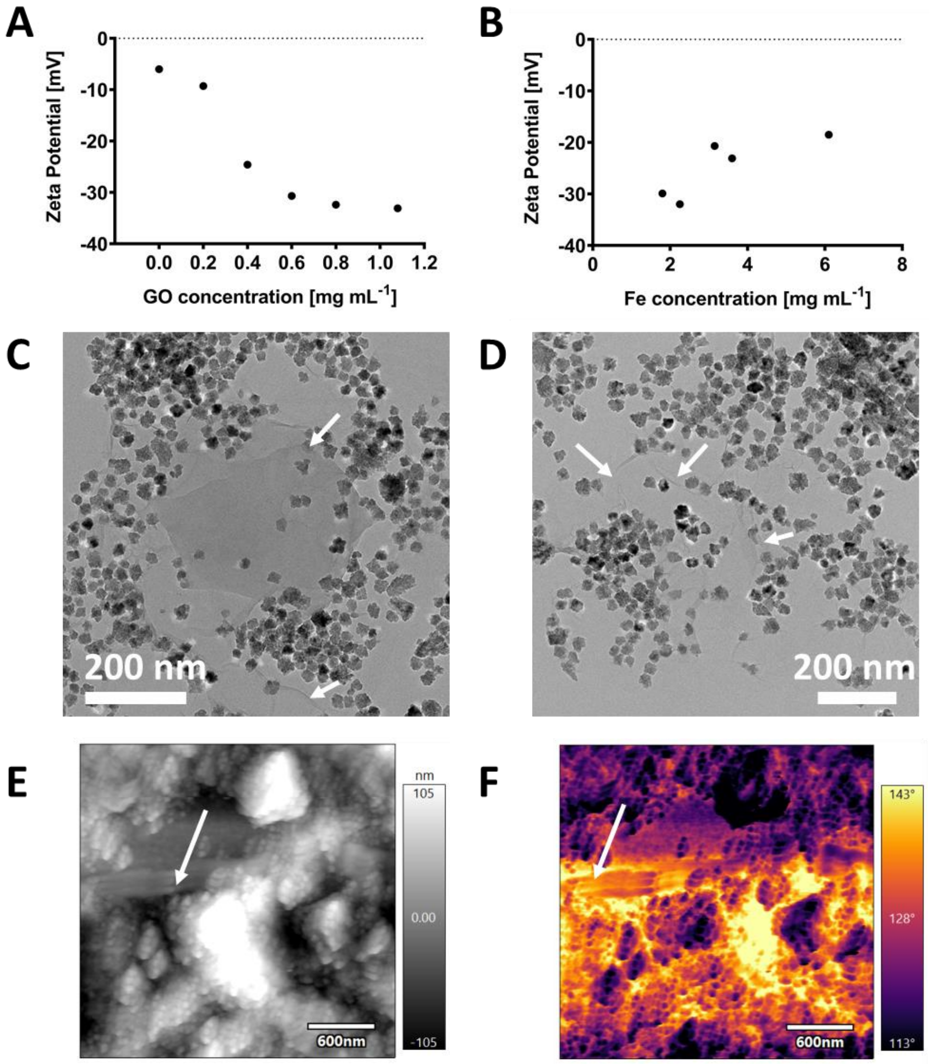

Figure 2. *Zeta potential of 150 times diluted sPNF_GO co-suspensions, recorded at pH 7, as a function of;* ***(A)*** *GO concentration (at Fe ~2.5 ± 0.2 mg mL^{-1} Fe), and;* ***(B)*** *Fe concentration (at GO 0.5 mg mL^{-1}). Representative TEM images of sPNF_GO (diluted 150-fold for drying) formed with;* ***(C)*** *Fe 3.6 mg mL^{-1} and GO 0.3 mg mL^{-1}, and;* ***(D)*** *Fe 3.6 mg mL^{-1} and GO 1.08 mg mL^{-1};* ***(E)*** *AFM and;* ***(F)*** *MFM images of sPNF_GO (diluted 100 times for drying) formed at Fe 3.6 mg mL^{-1} and GO 1.08 mg mL^{-1}. White arrows in (****C-F****) indicate position of GO flakes.*

2.2. AC-field hyperthermic efficiency of nanocomposite suspensions and gels

2.2.1. NF_GO suspensions

It is generally found that for MNP and NF syntheses that use conventional heating-up or polyol approaches the measured SAR values vary significantly from batch to batch (reflecting the stochastic nature of the nucleation process, and other factors that are difficult to control) [36, 37]. Furthermore, irrespective of the synthetic approach used, the 'native' SAR values (*i.e.* of single component NF suspensions) obtained can be concentration dependent (due to dipolar interactions, usually arising from partial aggregation) and the position of the thermal probe in the sample (due to inhomogeneity, or even partial precipitation, often associated with partial aggregation) [28]. In this study SAR was determined at ν_{AC} 535 kHz, I_{AC} 24 mT. The concentration dependencies of SAR were explicitly studied and care was taken to confirm sample homogeneity and stability of the measurements. The error given throughout for individual SAR measurements is *c*.5%, stemming from uncertainty in extracting the initial slope and the Fe concentration, see Methods. The SAR response of exemplar dispersions and hydrogels was also tested as a function of probe depth, it was found that all measured values fall within ±5% of the average for co-suspensions and ±2.5% for hydrogels, see Methods and Supporting Information (***Table S1***), confirming the absence of sedimentation.

Variability of the native SAR is well-known (if rarely discussed) and is difficult to avoid, hence we took the approach of preparing multiple NF batches for which the values were indeed found to vary (in the range 180-320 W g^{-1} with median around the 220 W g^{-1}) and evaluated the effect of NF and GO content on SAR for each batch. For multiple batches we observed and report consistent effects on SAR arising from varying the NF and GO content, irrespective of the native SAR. Hence the findings described are general and not related to the particular magnetic properties of any given NF batch. Note also that the heat capacity of H_2O was used in all SAR calculations presented in this study; the validity of this assumption for suspensions and gels is discussed below.

For sBNF and sPNF (single-component) suspensions, the measured SAR values are independent of the Fe concentration (***Figure 3A-B***). For the sBNF (bare NFs in suspension) batch shown in ***Figure 3A*** an average SAR value of 200 ± 10 W g^{-1} was obtained across a 40-fold NF concentration range. We also observe minimal effects of PEGylation on the SAR value for the single component suspensions, as expected for fully dispersed particles. Similarly for different sPNF (PEGylated NFs in suspension) batches, shown in ***Figure 3B***, a SAR value of 220 ± 4 W g^{-1} was obtained over a wide Fe concentration range. This also demonstrates that there is minimal effect of nanoflower concentration on the heat capacity of the suspensions, as expected given the dilution.

On the other hand for sBNF addition of GO flakes consistently led to a significant decrease of the (sBNF_GO co-suspension) SAR values, irrespective of the pH of the stable sBNF (bare NFs only suspension) used, *i.e.* pH 4 (***Figure 3C***) or pH 12 (***Figure 3E***), for which the native sBNF ζ_p values were +34 and -49 mV, respectively (***Figure S1B***). The observation of SAR suppression, irrespective of the sign of the BNF surface charge, suggests GO-induced BNF aggregation by hydrophobic interactions; hence this is most likely due to π-electron rich sp^2-hybridized regions on the planar GO surface interacting with γ-Fe_2O_3 sites inducing BNF-BNF interactions on-flake [38]. The inter-NF dipolar interactions incurred suppress the Néel contribution, which has been shown to dominate over any Brownian contribution for NFs [31]. On the other hand, we did not observe any SAR suppression for sPNF_GO (co-suspensions), irrespective of whether GO or NF concentration was varied (***Figures 3D*** and ***3F***); the SAR of these co-suspensions was independent of Fe concentration in this range. At constant GO concentration of 0.5 mg mL^{-1}, an average value of 213 ± 13 W

g^{-1} (***Figure 3F***) was measured, which is similar to the native SAR of this batch. Similar observations were made for three other independently prepared batches irrespective of their native SAR (***Figure S5***). These observations strongly support the interpretation that hydrophobic interactions generate partial aggregation in co-suspension for sBNF_GO, but not for sPNF_GO.

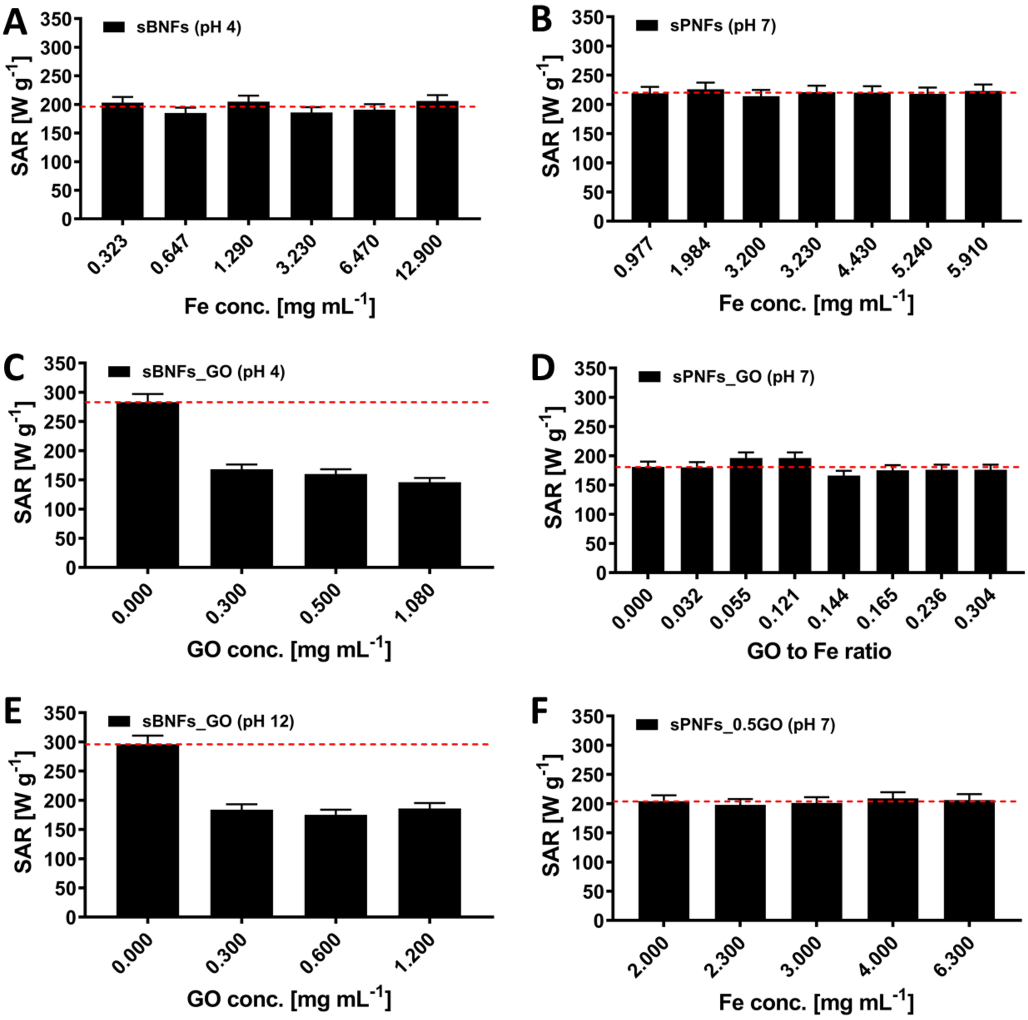

Figure 3. *Hyperthermic characterization of suspensions, ν_{AC} 535 kHz, I_{AC} 24 mT. SAR values (see Equation 1) for;* ***(A)*** *sBNF (bare NFs in suspension) at pH 4, and;* ***(B)*** *sPNF (PEGylated NFs in suspension) at pH 7 both as a function of Fe concentration;* ***(C)*** *sBNF_GO (co-suspensions) at pH 4 as a function of GO concentration;* ***(D)*** *sPNF_GO (co-suspensions) at*

pH 7 at Fe 3.5 ± 0.2 mg mL^{-1} as a function of GO concentration represented here as the GO to Fe ratio; ***(E)*** *sBNF_GO (co-suspensions) at pH 12 as a function of GO concentration at Fe 3.6 ± 0.4 mg mL^{-1}, and;* ***(F)*** *sPNF_0.5GO (co-suspensions at constant GO content) at pH 7 as a function of Fe concentration at fixed GO concentration of 0.5 mg mL^{-1}. Note; (i) each panel represents a different NF batch; (ii) repeat measurement confirming the generality of the findings and providing further experimental details are provided in* ***Figure S5****; (iii) the horizontal dashed lines indicate; for A-B the average SAR for the data in each panel; for C-F the native SAR value of the corresponding sPNF suspensions (without any GO). Error bar estimations are described in Methods.*

Note that the effect of GO, in the concentration range used, on the heat capacity of both suspensions and soft hydrogels of this type has been shown to be weak. For example, a marginal ~12%, decrease in heat capacity was shown on adding GO at 1 mg mL^{-1} to Pluronics-based gels [20]. A decrease in heat capacity induced by progressively increasing GO content would decrease the SAR value extracted (see Equation 1). For sPNF-GO co-suspensions, Figure 3D shows that there is no such decrease up to GO content of 1 mg mL^{-1}. Note that we have also demonstrated the lack of any AC-field induced heating for pure GO suspensions (***Figure S6***). In the next section, we describe consistent increases (SAR recovery) for nanocomposite hydrogels with increasing GO content, hence we can safely ascribe these changes to differences in inter-flower interactions mediated by GO flakes, not to changes in heat capacity.

2.2.2. NF_GO nanocomposite hydrogels

Considering the single-component gels, for a typical gBNF sample (gels with bare NFs, without GO, at pH 4), a SAR value of 50 ± 14 W g^{-1} was measured across the Fe concentration range (***Figure 4A***), which is a significant, 85%, suppression as compared to the equivalent sBNF suspension (native SAR 309 W g^{-1}). Similar suppression was noted for gBNFs in pluronics in our earlier study [24]. While for the equivalent gels with PEGylated nanoflowers, gPNF, (without GO, at pH 7) SAR decreased by only ~35% from 221 ± 3 to 145 ± 4 W g^{-1} and was independent of Fe concentration (***Figure 4B***). This indicates that PEGylation results in much better nanoflower dispersion during formation of PEO-PPO-PEO micelles. The advantages of PNFs over BNFs in the formation of useful AC-field responsive nanocomposite gels, irrespective of possible mitigation provided by GO, are clear.

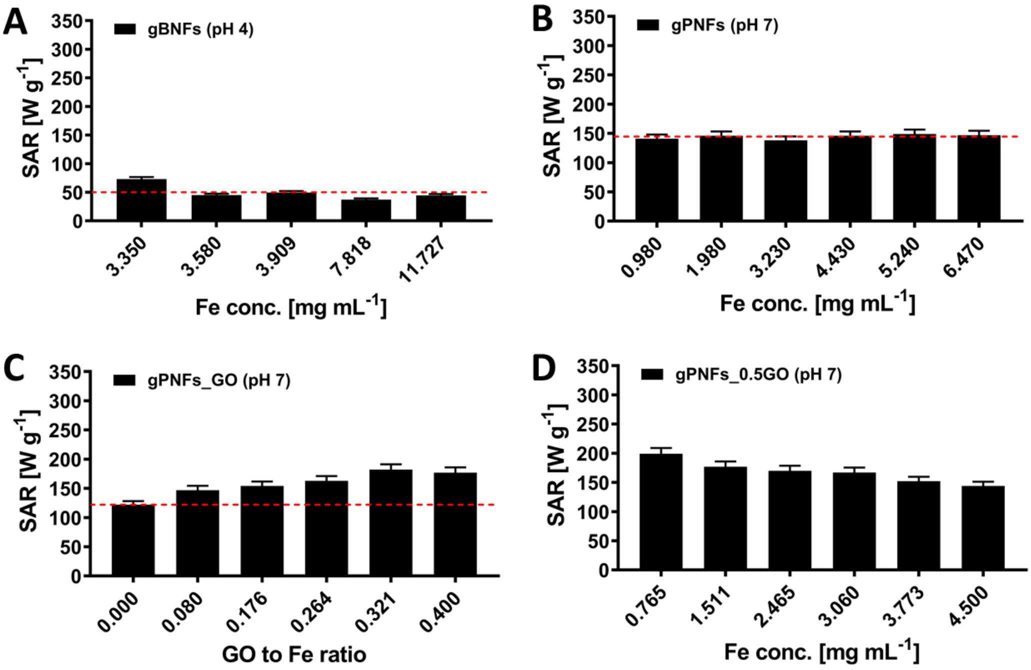

Figure 4. *Hyperthermic characterization of nanocomposite gels,* ν_{AC} *535 kHz,* I_{AC} *24 mT. SAR values for;* ***(A)*** *gBNF (bare NFs in gels) prepared from an sBNF suspension at pH 4, and;* ***(B)*** *gPNF (PEGylated NFs in gels) prepared, as per Scheme 1B, from an sBNF suspension at pH 7, both as a function of Fe concentration;* ***(C)*** *gPNF_GO (nanocomposite GO-PEGylated NFs gels) at pH 7 at Fe 3.1 ± 0.2 mg* mL^{-1} *as a function of GO concentration, represented here as the GO to Fe ratio;* ***(D)*** *gPNF_0.5GO (nanocomposite GO-PEGylated NFs gels at constant GO content) at pH 7 as a function of Fe concentration at fixed GO*

concentration of 0.5 mg mL^{-1}. Note; (i) all gels were prepared in 40 w/v% F127 see ***Table 1****; (ii) each panel represents a different NF batch; (iii) repeat measurement confirming the generality of the findings and providing further experimental details are provided in* ***Figure S7****; (iv) 3 data points in A were reproduced from reference [24]; (v) The horizontal dashed lines indicate; for A-B the average SAR values for the data in each panel; for C-D the SAR value of the corresponding gPNF samples (hydrogel without any GO).*

Turning to the two-component gels, for gBNF_GO samples inconsistent SAR dependencies were observed on progressively increasing GO content for different batches of similar native SAR. Hence the hyperthermic responses of these gels are not shown. We speculate that these differences arise from intermediate scale inhomogeneities that are sensitive to the initial mixing of the suspensions due to complex interactions between the multiple components present.

On the other hand, for PEGylated NFs consistent hyperthermic responses were obtained. SAR values were measured for gPNF_GO as a function of GO to Fe ratio at constant NF concentration (Fe 3.1 ± 0.2 mg mL^{-1}, ***Figure 4C***), and at constant flake concentration (GO 0.5 mg mL^{-1}, ***Figure 4D***). The SAR for the gPNF batch (without GO) used to generate these two plots was 122 W g^{-1} as indicated in ***Figure 4C***, and the native suspension value (without GO) was 188 W g^{-1}. SAR was found to progressively increase with addition of GO flakes up to 182 W g^{-1} at GO/Fe *c.*0.32 (corresponding to 2.5 mg mL^{-1} Fe and 0.80 mg mL^{-1} GO), *i.e.* the SAR of the nanocomposite gel recovered to a value similar to that of the native GO-free suspension. The fact that it is possible to almost fully recover the native suspension SAR for gPNF_GO demonstrates again that any contribution from Brownian processes to the hyperthermic responses of NFs is negligible [31]. It also again shows that it is a reasonable approximation to use the heat capacity of H_2O in calculating SAR for the nanocomposite gels.

Similar SAR measurements as a function of GO were performed on three other independent PNF batches with varying native SAR values (***Figure S7***). A consistent increase in SAR with increasing GO content was observed irrespective of the native SAR, with all batches reaching a maximum (batch dependent) value at GO/Fe in the range of 0.3-0.38 (corresponding to 1.08 mg mL^{-1} GO). This confirms that higher GO content is invariably associated with recovery of higher SAR values, to close to that of the corresponding sPNF_GO co-suspensions (***Figures 3D*** and ***S5***). The effect of GO on the gels is also clearly demonstrated by comparison of sPNF_GO (***Figure 3F***) in which case the SAR is independent of GO concentration with gPNF_0.5GO (***Figure 4D***) in which case SAR decreased with increasing Fe concentration over the same Fe concentration range. Note co-suspensions and nanocomposite gels with GO > 1.20 mg mL^{-1} were difficult to prepare due to constraints on initial NF and GO concentrations in the master batches, and co-suspension stability at higher concentrations.

In summary, it is clear that GO-induced interactions with PPO segments reducing inter-PNF interactions, and hence inter-flower dipolar coupling, are a general feature of this nanocomposite gel system. Within the gels the presence of the GO flakes alters the molecular interactions and hence the arrangement of the nanocomposite components. We suggest that hydrophobic attraction between the PPO blocks in F127 and the exposed GO surface decreases the potential for non-cohesive interactions between PNFs and those PPO blocks. GO-induced higher SAR values measured at lower Fe concentration, as compared to the GO-free case, strongly support increasingly cohesive (hydrophilic) PNF-F127 interactions, preventing inter-flower dipolar coupling which would reduce hyperthermic efficiency [30].

To our knowledge there is only one related report of the effect of MNPs and GO on hyperthermic responses in gels. Le *et al.* [39] investigated magnetic manganese ferrite MNPs immobilized onto GO. This system is complicated as MNP binding was described as increasing the magnetic anisotropy (increasing SAR), while gelation was suggested to decrease the Brownian contribution which, unlike NFs, is significant for spherical particles in this size range. Differences in the concentration-dependencies of SAR were also described for free- and GO-immobilized MNPs in suspension demonstrating that aggregation (which was reported to differ for MNP and MNP-GO) suppresses SAR. Hence the responses were complex. This study is complementary to ours, confirming the key roles of motional restriction and aggregation in determining hyperthermic responses. However, in our approach the interactions between the components within the nanocomposite gels are simplified. Our observations are consistent with the absence of direct PNF-PNF or PNF-GO interactions in the gels, which are hard to avoid when the particles are bound to the flakes. Hence our approach identifies the potential for SAR recovery arising from compositing the two components independently.

2.3. Spatiotemporally specified AC-field induced heating in patterned PNF_GO nanocomposite hydrogels

Finally, following our initial report of AC-field induced heating in structures printed using gBNFs as the magnetically-responsive ink [24], a preliminary evaluation of the printability of gPNF and gPNF_GO and the responses of the prints was undertaken. In all cases the nanocomposite gels were found to be shear-thinning and printable and, as expected, the presence of GO improved the AC-field response. It was observed (***Figure 5, Figure S8***) that samples with and without GO provided smooth prints using a standard extrusion format without significant optimization, and the deposited material showed good structural integrity

(***Figure 5***). The average feature thickness (FT) of GO containing prints (all at Fe 2.5 ± 0.2 mg mL^{-1}) obtained using a 150 µm (ID) needle were measured to be 155 ± 15, 244 ± 18, 154 ± 15 and 231 ± 13 µm for gPNF, gPNF_0.6GO, gPNF_0.8GO and gPNF_1.08GO, respectively (***Figure S9***). While there was some spreading for gPNF_0.6GO and gPNF_1.08GO, it is clear that process optimization should enable high-fidelity printing (FT=ID) for nanocomposite inks from across this range of formulations (by identifying the ideal pressure/feed rate, needle diameter, humidity, temperature) although given the number of relevant parameters that is beyond the scope of this study. Interestingly, this variation reveals FT-dependent heat dissipation effects relevant to practical applications, see below.

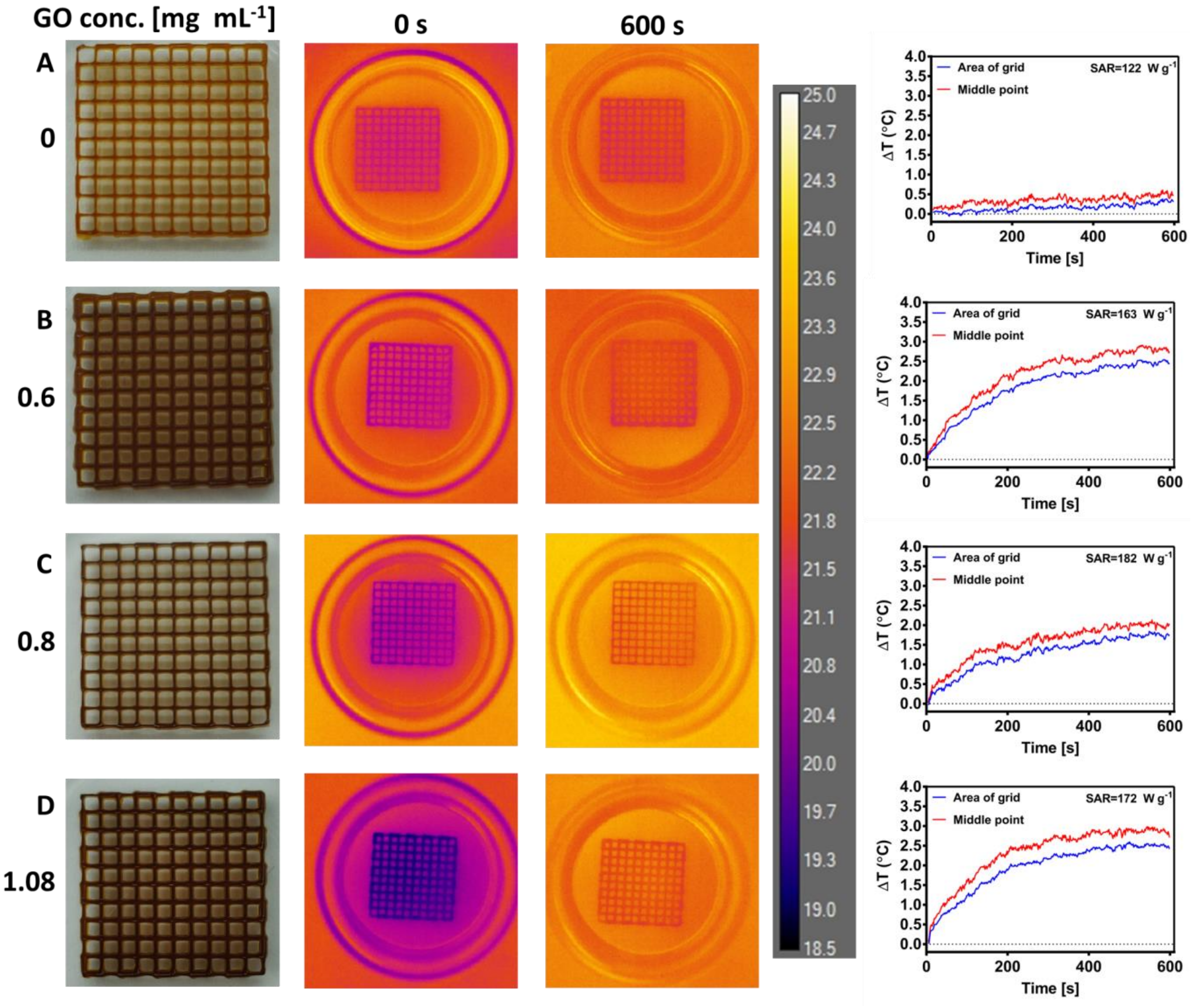

Figure 5. *Thermographic evaluation of spatially patterned/3D printed gPNF_GO grids at Fe 2.5 ± 0.2 mg* mL^{-1}*;* ***(A)*** *gPNF;* ***(B)*** *gPNF_0.6GO;* ***(C)*** *gPNF_0.8GO, and;* ***(D)*** *gPNF_1.08GO. From the left; optical photographs of each 1.5 cm x 1.5 cm x 1 mm (high) print; time resolved in-situ thermography of 'open system' LC-AMF stimulation (*ν_{AC} *663 kHz,* I_{AC} *16 mT) of printed grids at the start (0 s, and ~19°C in all cases) and at the end (600 s) of the irradiation, a single colour-coded thermal scale is used for all thermographs; the change in temperature (ΔT) as a function of irradiation time (as a whole grid average and at the centre point), the closed system SAR values of the gels are indicated. The error in temperature is <0.1 °C in all cases, see Methods.*

In the case of gPNF (without GO) the hyperthermic response (evaluated at higher frequency, ν_{AC} 663 kHz, and lower field strength, I_{AC} 16 mT, than for the previous measurements, see Methods) was weak, with an increase in temperature after 600 s, ΔT_{600s}, of ~0.4 °C observed (***Figure 5A***), as we have previously observed [24]. Upon addition of GO a significant increase in response was observed, with ΔT_{600s} of ~2.5 °C at the plateau for gPNF_0.6GO (***Figure 5B***) and gPNF_1.08GO (***Figure 5D***). A weaker response was observed for gPNF_0.8GO (***Figure 5C***), even though its native SAR was slightly higher, due to greater dissipation associated with smaller FT and hence higher surface area (***Figure 5*** and ***Figure S9***). Interestingly, for the three GO-containing prints shown in ***Figure 5***, the extracted initial slope (the average for the whole grid area, blue curves in ***Figure 5***), or $\Delta T/\Delta t_0$, is independent of GO content, with an average value of 0.012 ± 0.001 °C s^{-1} obtained. Note that this is for samples of similar native SAR and the same Fe concentration. We have not scaled $\Delta T/\Delta t_0$ by Fe content to generate a 'SAR' value due to the slightly different ν_{AC} and I_{AC}, as compared to that used to collect the data in ***Figures 3*** and ***4***, of the open-coil geometry used for imaging and the differences in heat dissipation incurred by this format.

These observations demonstrate that for printed nanocomposite gels; (*i*) the initial AC-field heating response (at close-to adiabatic conditions) is largely independent of both GO and FT; (*ii*) the temperature jumps, ΔT, obtained are similar, in this Fe concentration range, for GO $\geq$ 0.6 mg mL^{-1}; (*iii*) the FT value largely determines the dissipation and hence the ΔT that can be achieved which sets a lower, Fe-dependent, limit on FT, and most critically; (*iv*) in our earlier thermography study of BNFs in similar 10 x 10 printed pluronics F127 grids realising a ΔT_{600} of ~6 °C required an Fe concentration of 140 mg mL^{-1} [24], compromising applications. Here ΔT_{600} of ~2.5 °C is observed at only 2.5 mg mL^{-1} (***Figure 5***), at face value this is an efficiency enhancement of 23-fold. PEGylation and nanocompositing with GO contribute to this improvement in the applications relevant format, without compromising printability for pluronics-based hydrogels.

3. Conclusions

In summary, we investigated the effects GO flakes in the size range of 240 ± 20 nm, on magnetic nanoflower particle suspensions and nanocomposite gels formed with F127. In particular we distinguished favourable and disruptive cases of nanocompositing with GO flakes, depending on the surface coating of NFs. For bare nanoflowers (BNFs), addition of GO led to a decrease of SAR, both in suspension and in nanocomposite gels, driven by hydrophobic interactions of NFs with the sp^2-hybridized regions on GO surface that generate inter-flower dipolar coupling. Addition of GO flakes to suspensions of PEGylated nanoflowers (PNFs) had no effect on the SAR, indicating a lack of disruptive mechanisms and associated inter-PNF interactions. On the other hand, increasing GO content in the nanocomposite hydrogels progressively increased cohesive hydrophilic interactions, reducing PNF dipolar coupling and leading to recovery of SAR, as compared to the equivalent gels without GO, to values close to the native suspensions. Hence PEGylating and incorporation of GO provided nanocomposite hydrogels that retain significant greater hyperthermic efficiency than was previously possible, enabling use of much lower (approximately 23-fold) NF concentration to achieve any target hyperthermic response (temperature jump). Finally, we show that gPNF and gPNF_GO hydrogels are both homogenous on a macroscopic level and are printable for a variety of applications including as remote AC-field responsive spatially-patterned heating components, *e.g.* for controlled release in tissue engineering or other release applications. Hence this study will contribute to the development of design rules for patternable magnetic hydrogels, for which simple chemical modification (introduction of nanofillers such as GO and/or use of PEGylation) provides cohesive interactions maintaining dispersion of nano-components. This provides sample homogeneity and optimal rheology while allowing increasing fraction of the responsive component in the nanocomposite. Strategies of this type will provide improved materials for personalized and autonomous tissue engineering systems, for instance as next-generation spatiotemporally-responsive supports for tissue engineering [40, 41].

4. Materials and Methods

Chemicals: Sigma-Aldrich (Merck:) diethylene glycol (99%), *N*'methyldiethanolamine (≥99%), ethyl acetate (≥99.5%), diethyl ether (≥99.5%), polyethylene glycol, tetrahydrofuran (≥99.9%), gallic acid (≥97.5%), 4-dimethylaminopyridine (≥99%), *N*,*N*'-dicyclohexylcarbodiimide (99%), Pluronics P127, deuterated chloroform (≥99%) and AAS Fe Standard (1001 mg L^{-1} ± 4 mg L^{-1}). Honeywell: iron (III) chloride hexahydrate (≥99%), iron (II) chloride tetrahydrate (≥99.0%), nitric acid (≥65%) and hydrochloric acid (≥37%). Fisher Scientific: sodium hydroxide (99.4%) and chloroform (≥99%). VWR chemicals: iron (III) nitrate nonahydrate (100%). Chempur, Poland: sulfuric acid H_2SO_4 (≥99%), hydrogen peroxide H_2O_2 (≥99%) and potassium permanganate $KMnO_4$ (≥99%).

Preparation of graphene oxide flakes: In order to obtain reduced graphene oxide, the graphite oxidation was performed utilizing modified Hummer's method, as previously reported [42, 43]. In brief, 30 g of graphite flakes ranging in diameter from 125 to 150 μm (Asbury Carbons, USA) was poured into beaker with solution of 17 g of potassium nitrate (KNO_3 Chempur, Poland) in 2 L of sulfuric acid (95%, H_2SO_4) and thoroughly mixed. The beaker with reagents was then put into water/ice bath, and 180 g of potassium permanganate ($KMnO_4$) was gradually added into the mixture. After last portion of oxidant was added, the beaker was taken from the bath and kept for 3 h at 30–35 °C with continuous stirring. Then it was left at room temperature (25 °C) for two days. After that time, the deionized water was carefully added to the mixture, so its temperature had not exceeded 35 °C. In the next step, the acid–graphite oxide mixture was heated to 95 °C, while stirred vigorously, and kept under these conditions for 15 min. The heater was then turned off and allowed to cool down slowly. Oxidation process was performed for a several hours, and eventually stopped by the addition of deionized water and hydrogen peroxide (30% H_2O_2). The graphite oxide mixture was purified by centrifugation (Thermo Lynx 4000, Osterode, Germany). It was then sonicated for 1 h with ultrasonic processor (Sonics and Materials INC, VCX750, Newtown, CT, USA) to exfoliate graphite oxide, thus obtaining graphene oxide.

Elemental combustion analysis: Elemental analysis was performed using combustion analyzers: CHN628 and OH836 (Leco). CHN628 analyzer was used for detection of carbon, nitrogen and hydrogen, whereas OH836 analyzer was used for oxygen estimation in helium atmosphere. Prior to examination, apparatuses were calibrated with calibration samples delivered by the analysers' producer – in case of CHN628 analyzer, two calibration samples with strictly defined content of specified elements were used, namely: EDTA (composed of 41.09 ± 0.23 % carbon, 5.51 ± 0.05 % hydrogen and 9.56 ± 0.04 % nitrogen) and BBOT (containing 41± 0.48 % carbon, 1 ± 0.10 % hydrogen, 6.43 ± 0.12 % nitrogen). Second analyzer was calibrated with two standards: silicon dioxide and iron (III) oxide, both with strictly defined compartment of oxygen: 53.05 ± 0.5 % in case of silicon dioxide and 30.02 ± 0.4 % for iron (III) oxide respectively. As experimental protocol requires small masses of samples, 0.005 g and 0.01 g sample's weight were used (microbalance – Sartorius Quintix). Elemental analysis of final GO composition is 41% C, 48.3% O, and <1% H and N.

Raman spectroscopy: Raman measurements were performed on Renishaw inVia Raman Microscope using 532 nm wavelength obtained from Nd:YAG laser. The laser was focused on sample using x100 objective and numerical aperture NA=0.9 in a backscattering geometry. The size of laser spot was about 0.5 μm with an average power of laser about 5 mW. An integration time of 3 s was used, and 15 accumulations were taken for each spectrum. Measurements were performed at room temperature. Baseline was created and subtracted in Origin Pro 2021b.

Scanning electron microscopy (SEM) of GO flakes: The GO water dispersion of 0.5 mg mL^{-1} was drop casted on a silicon substrate and then dried 24 hours at 40 °C. Flakes were visualized using Auriga (Zeiss) SEM microscope with the backscattered electron (BSD) mode with a detector set to 0.5 kV.

Magnetic nanoflower (NFs) preparation: Synthesis of iron oxide nanoflowers was based on forced hydrolysis of iron chloride precursors by the polyol route, which was adapted from Hugounenq *et al.* [32]. Briefly, in a typical preparation Iron (III) chloride hexahydrate (0.541 g, 2 mmol), Iron (II) chloride tetrahydrate (0.199 g, 1 mmol) were dissolved in a DEG/ NMDEA mixture (37.1 mL, 1:1 v/v) in a 100 mL round bottom flask. A wide range of conditions have been reported [32, 44], in selecting this solvent ratio and other conditions we followed the protocol from Hugounenq [32], which provides a detailed analysis of the effect of the key parameters. Separately, sodium hydroxide (0.32 g, 8 mmol) was dissolved in a DEG/NMDEA mixture (19 mL, 1:1 v/v). This solution was then added to the solution of iron chlorides and stirred for 3 hrs. Then, the temperature was increased to 220 °C at 5 °C min^{-1} by placing the round bottom flask in temperature-controlled heating mantle. The suspension was heated with magnetic stirring for 12 hrs, and then allowed to cool to room temperature. The black sediments were separated magnetically and washed with an ethanol/ethyl acetate mixture (1:1 v/v) for 3 times to remove impurities. Possible iron hydroxides were removed by treatment with 10% v/v nitric acid (10 mL). Iron (III) nitrate nonahydrate (4.125 g) was dissolved in water (10 mL) and added to the nanoparticles suspension. The resulting mixture was heated to 80 °C for 45 mins to ensure complete oxidation of the nanoparticles, to $\gamma\text{–}Fe_2O_3$. After another treatment with 10% v/v nitric acid, the suspension was washed twice with acetone and diethyl ether and re-dispersed in desired amount of water.

PEG-Gallol synthesis: This synthesis was adapted from a method by Studart *et al.* [33]. Poly (ethylene glycol) (PEG) (4 g, 0.5 mmol, 8000 g/mol) was dissolved in tetrahydrofuran (THF) (70 mL) in the round bottom flask. When the PEG was fully dissolved, through sonication (20-30 mins) and mild heating (≈ 30 °C), Gallic acid (0.084 g, 0.5 mmol) was added to the round bottom flask. Separately, 4-Dimethylaminopyridine (DMAP) (0.009 g, 0.073 mmol) was also dissolved in THF (1 mL) and then added to the round bottom flask. The solution in the round bottom flask was then magnetically stirred at room temperature. *N*,*N*'-Dicyclohexylcarbodiimide (0.5256 g, 2.5 mmol) was then dissolved in THF (5 mL) and added slowly to the solution stirring in the round bottom flask. The solution was left to stir at room temperature for 19 hrs. After this time had elapsed, the round bottom flask was fitted to a rotary evaporator, where the solvent was removed. Deionized H_2O (200 mL) was added to the remaining solid. This aqueous solution was stirred/sonicated to redissolve the solid. The pH was adjusted to 2 using 1 M HCl (~2 mL) and was then allowed to sit for 1 hr. The solution was centrifuged (5500 rpm for 10 mins) and the pellet (urea by-products) was discarded. The product was extracted from the aqueous phase with $CHCl_3$. $CHCl_3$ was removed and the product was dried under N_2. The typical yield was *c.*70%.

PEGylation of NFs: For preparation of PNFs, 1:1.75 mass ratio of BNFs to PEG-Gallol was used. We established this as a sufficient PEG-Gallol concentration leading to a full coverage of BNFs surface and full stability across all pH values, as shown in ***Figure S1***. The stability of these suspensions over the pH range were done using the suspension titration with 0.05 mM HCl and 0.05 M NaOH solutions. At each titration addition, the sample was vortexed for 45 sec.

^{1}H nuclear magnetic resonance (NMR) spectroscopy: NMR spectra were recorded on a Varian VnmrS (500 MHz) spectrometer. The synthesized PEG8000-Gallol was dissolved in deuterated chloroform ($CDCl_3$) solvent and a drop of trimethyl silane (TMS) was added as an internal standard to measure the intensity of proton peaks in the compound. NMR spectra were analyzed using MastreNova 6.0.2 software © 2009 Mastrelab Research.

Fabrication of nanocomposite suspensions and hydrogels: GO flake solution (0.0 to 1.08 mg mL^{-1}) and PEGylated (or bare) NFs (at required concentration) were firstly stabilized separately at pH 7 by titrating with 0.05 M HCl and/or 0.05 NaOH solutions. After stabilizing at pH 7, GO and PNFs were mixed using a vortex and made into 1 mL nanocomposite suspension (sPNF_GO) using HPLC grade H_2O. 0.4 g (40 w/v%) of Pluronics P127 was added to the suspension and homogenized by cycling from room temperature to 4 °C (2 min) to room temperature till it dissolved. We formed a stable nanocomposite hydrogel (gPNF_GO) at room temperature after a cooling cycle under refrigeration (at 4 ˚C for 24 hrs).

Dynamic light scattering (DLS) and zeta potential: Measurements were performed at 25 °C on a Malvern NanoZS (Malvern Instruments, Malvern UK) instrument, which uses a detection angle of 173°, and a 3 mW He-Ne laser operating at a wavelength of 633 nm. The Z-Average (mean hydrodynamic) diameter, d_{hyd}, and the polydispersity index (PDI) values were obtained from analysis of the correlation functions by cumulants analysis using the Dispersion Technology software (v. 4.10, Malvern Instruments; Worcestershire, U.K.). For all measurements, samples were diluted to 0.5 mM (0.028 mg mL^{-1}) concentration of Fe. For zeta potential measurements, the pH of GO suspensions and sPNF_GO were adjusted by the additions of 0.05 M NaOH.

Transmission electron microscopy (TEM): Images were acquired on a Hitachi transmission electron microscope at an accelerating voltage of 100 kV. Samples were prepared by pipetting 7 μL of the aqueous suspensions on to a Formvar coated copper grid and allowing drying naturally overnight. Data analysis was done using ImageJ software and >100 particles were manually counted to obtain the average size.

Scanning electron microscopy – electron dispersive X-ray spectroscopy (SEM-EDX) of gPNF_GO hydrogels: Prior to imaging, the hydrogels were flash-frozen in liquid nitrogen and lyophilized to form freeze-dried solids. These were carefully cut into small porous particles that were coated with a 7.5 nm layer of Iridium using a Quorum Technologies Q150T ES sputter coater. These samples were then imaged using a Hitachi Regulus 8230 scanning electron microscope. EDX was performed using an Oxford Instruments Ultim max 170. Measurements and elemental maps of freeze-dried gPNF and gPNF_GO gels (***Figure S4***) have an associated penetration depth of *c.*1 μm.

Magnetic hyperthermia: Measurements on bulk homogeneous samples were carried out using a NanoTherics NAN201003 MagneTherm^{TM} AC-field generator (NanoTherics Ltd.; Newcastle-under-Lyme, United Kingdom). The system allows measurement of temperature vs time via a non-metallic OP-Sens optical thermometer to avoid eddy currents. Typically, 1 mL of sample was transferred into a plastic cylindrical shape 2 mL Eppendorf tube with a whole on a cup that fits well the optical thermometer probe. The sample was placed in a thermally insulating polystyrene sample holder to maintain close-to-adiabatic conditions. The sample temperature was measured by Fibre Optic Probe (Opsens Ltd., Canada), typically fitted at the bottom of the 1 mL sample. This was chosen based on measurements at different depths for NFs at positions 5, 10, 15 and 20 mm from the upper surface of the 20 mm (1 mL) deep samples (see supporting information, ***Table S1***). The temperature of the sample was equilibrated in the instrument before the desired field was applied. Unless otherwise noted, measurements were carried out at a frequency of 535 kHz and magnetic field strength of 24 mT. These will be referred to as 'closed system' measurements. For each SAR determination, the error of the initial slope fitting is estimated as standard error calculated using OriginPro, providing average uncertainty of ~4%. We used a fourth order polynomial, increasing that to fifth order had no discernible effect on the linear term. The error in determining the concentration of Fe using AAS is estimated to also be ~2.5%. Combined these give an estimated error in SAR for each measurement of ~5%. This is represented as error bars in Figures 3 and 4 and as ± in the text.

Elemental analysis using atomic absorption spectroscopy (AAS): The elemental analysis of iron was performed by digesting 40 μL of a stock solution in 1.5 mL concentrated HCl (12 M) and kept for 2 hrs till all iron dissolved in HCl. These samples were further diluted to 50 mL with 1 M HNO_3 using a volumetric flask. AAS was performed on Varian spectra AA 55 B atomic absorption spectrometer.

Atomic force microscopy: For AFM studies, PNFs and sPNF_GO were diluted in distilled water to 1:100 range just before use and immediately drop casted onto an ITO-coated glass surface. The samples were imaged in air using an MFP-3D AFM system (Asylum Research). Imaging was performed in amplitude modulation mode and height, amplitude, and phase images were recorded. Data were recorded with 256 lines per scan direction and with a scan rate of 0.7 Hz. For MFM studies, magnetically coated silicon AFM probes (ASYMFM from Asylum Research) were used. ASYMFM probes have a cantilever length of 240 μm with a resonant frequency of ~75 kHz and a typical spring constant of 3.5 N m^{-1}. The magnetic coating consists of approximately a 50 nm layer of Co/Cr alloy. To ensure a predominant orientation of the magnetic field vector along the major axis of the probe, the ASYMFM probes were magnetized prior to taking measurements by subjecting them to the field of a permanent magnet for 10 s. MFM experiments were recorded by the topographic (main) scan with the 'Lift Mode' scan, in which the AFM tip was made to scan the sample at lift heights of 50 nm above the sample surface. AFM height images were recorded using the topographic scan lines while the amplitude and phase images were recorded using the lift-mode scan lines. All MFM images were flattened and presented with no further processing. The GO sample was spin coated on a Si/SiO$_2$ (300 nm) substrate using a POLOS spin coater. The silicon substrates were first cut into 1 cm^2 pieces, cleaned in acetone, DI water and ethanol by the aid of sonication and the oven dried. The GO water dispersion of 0.5 mg mL^{-1} was then deposited using a speed of 3000 rpm and an acceleration of 300 rpm s^{-1} to cover Si/SiO$_2$ with monolayered GO flakes. AFM measurements of GO were then performed using the Icon Scanning Probe Microscope (Bruker). Samples were scanned in air, at room temperature using tapping mode with antimony n-type doped Si (RTESP-300, f: 300 kHz, 40 N m^{-1} – Tapping mode) tips. The images were acquired at 512 × 512 pixels resolution at a scan rate between 0.5 and 0.75 Hz and 2nd order flattened using Nanoscope software (***Figure S2***).

Rotational rheological: The rheology was performed on Physica MCR301 rheometer from Anton Paar. Parallel plate geometry with a 25 mm diameter top plate and, unless otherwise stated, 0.5 mm gap was used. About 200 μL of sample was placed on the bottom plate using a spatula, and subsequently the top rheometer plate was lowered slowly to minimize hydrogel disruption for each measurement. All viscosity-shear rate experiments (flow curves) were performed at 19 °C, with samples subjected to shear rate from 0.01 s^{-1} to 2000 s^{-1}, and being held at each shear rate until a stable reading was reported by the instrument.

3D printing: Printability of hydrogels was performed using dual-head Allevi-2 bioprinter. In order to load inks into printing syringe, samples were kept in the fridge for <30 mins, removed from refrigerator and immediately transferred as liquids (4 °C) in the syringe and immediately returned to refrigerator for 10 mins to remove any potential bubbles. Then, prior to printing, syringes were finally rested at 19 °C for 30 mins. Each gel was printed into a 15 x 15 mm grid, using a straight stainless-steel needle with 152 µm inner diameter. Different head velocities 200 - 300 mm.min^{-1} and pressures 5.24 - 5.65 bar were used for different formulations, all parameter ranges used are summarized in ***Table 2*** below. The gcodes used to print the grids are provided in ***Table S2***. Finally, captured photographs were analysed using ImageJ to establish thickness of lines within printed grids, based on at least 9 measurements across both X and Y grid thicknesses, represented in main text as averages ± standard deviation.

Table 2. Description of parameters used for printing purpose

Parameters	**Symbol**	**Values**
Head temperature	T	19 ± 0.5 °C
Needle length	L	12.7 mm
Needle inner diameter	D	152 µm
Extrusion pressure	Δp	5.24-5.65 Bar
Extrusion velocity	ν	200-300 mm min^{-1}
Distance from the substrate	Z	0.7-1 mm

In situ thermal imaging during alternating magnetic field (LC-AMF) irradiation: Measurements were carried out on a Live Cell–Alternating Magnetic Field (LC-AMF^{TM}) module connected to a NanoTherics NAN201003 MagneTherm^{TM} system, which enables RF irradiation of a sample placed in a standard glass Petri dish (of diameter *d*=35 mm). Measurements were carried out at a frequency of 663 kHz and magnetic field strength of 16 mT. Thermal imaging was performed using a Flir A655sc thermal camera (Flir, Butler Technologies). The camera was aligned to view samples carefully placed in a 35 mm glass Petri dishes from top. Recordings were made for 10 mins and the LC-AMF was turned on immediately after the recording started. Each 10 mins recording consists of 3750 frames at 6.25 Hz. The resolution of the A655sc camera is ~170 µm (pixel size). The whole setup was placed in a dark room to minimize IR reflections and temperature fluctuations during imaging. These will be referred to as ‘open system’ measurements. The thermal camera detects temperature differences down to <30 mK, even at a longer working distance. Considering the effective pixel size, the temperature error on each pixel is therefore expected to be <0.1 ^{o}C. The internal calibrations, or Non-Uniformity Corrections, accord to ISO9001:2008 as detailed at https://www.flir.com/support-center/Instruments/service/calibration-technical-data/.

Supporting Information

The Supporting Information is available free of charge at https://

NMR of synthesized PEG-Gallol; Characterization of MNFs; characterization of GO; SEM-EDX characterization of gPNF_GO hydrogels; SAR evaluation of other batches for control GO flakes, sPNF_GO and gPNF_GO; supporting pre- and post- 3D printing characterization. (PDF), Gcodes for printing grids.

Acknowledgements

We thank Dr. Ian Reid from the Nano Imaging and Material Analysis Centre for supporting SEM imaging.

Funding Sources

The authors acknowledge support from Science Foundation Ireland (16/IA/4584 and 17/CDA/4637). The graphene oxide synthesis and characterization was financially supported by Łukasiewicz Research Network - Institute of Electronic Materials Technology statutory grant no-S2-10-1019-20.

Notes

The authors declare no competing financial interest. All research data supporting this publication are directly available within this publication and associated supporting information.

Authors' statement

E. R. A. Prepared samples, performed DLS, zeta potential, closed system hyperthermic and AAS measurements.

E. G. Synthesized NFs and PEG-Gallol. Prepared samples, performed DLS, zeta potential and hyperthermic measurements.

K. S. Synthesized NFs; performed 3D printing & rheological measurements and supported LC-AMF measurements.

S. K. Performed AFM/MFM measurements of sPNF and sPNF_GO.

K. K. Synthesized and characterized GO.

S. S. Synthesized NFs. Performed TEM.

E. M^{c}K. Determining NMR yields; NMR analysis; Synthesized NFs; Repeat measurements of zeta potential and assisting with the improved text for the synthetic methods.

C. M. Determining NMR yields, NMR analysis, Synthesized NFs; Repeat measurements of zeta potential and assisting with the improved text for the synthetic methods.

K. M. Synthesized NFs; Repeat measurements of zeta potential and assisting with the improved text for the synthetic methods.

L. J. Synthesized NFs

B. J. R. Supported AFM/MFM measurements. Supervision. Funding acquisition. Validation.

D. F. B. Designed the study. Prepared initial and final draft of the manuscript. Supervision. Funding acquisition. Validation.

J. K. W. Designed the study. Performed AFM of GO sample and LC-AMF measurements. Prepared initial draft and final version of the manuscript. Supervision. Validation.

ORCID numbers of authors

Krystian Kowiorski: https://orcid.org/0000-0003-3857-3413

Brian J. Rodriguez: https://orcid.org/0000-0001-9419-2717

Dermot Brougham: https://orcid.org/0000-0002-1270-8415

Jacek K. Wychowaniec: https://orcid.org/0000-0002-6597-5242

References

[1] E.K. Fox, F. El Haddassi, J. Hierrezuelo, T. Ninjbadgar, J.K. Stolarczyk, J. Merlin, D.F. Brougham, Size-Controlled Nanoparticle Clusters of Narrow Size-Polydispersity Formed Using Multiple Particle Types Through Competitive Stabilizer Desorption to a Liquid-Liquid Interface, Small 14(44) (2018).

[2] J.K. Stolarczyk, A. Deak, D.F. Brougham, Nanoparticle Clusters: Assembly and Control Over Internal Order, Current Capabilities, and Future Potential, Advanced Materials 28(27) (2016) 5400-5424.

[3] M.K. Jaiswal, M. De, S.S. Chou, S. Vasavada, R. Bleher, P.V. Prasad, D. Bahadur, V.P. Dravid, Thermoresponsive Magnetic Hydrogels as Theranostic Nanoconstructs, ACS Applied Materials & Interfaces 6(9) (2014) 6237-6247.

[4] B.T. Mai, P.B. Balakrishnan, M.J. Barthel, F. Piccardi, D. Niculaes, F. Marinaro, S. Fernandes, A. Curcio, H. Kakwere, G. Autret, R. Cingolani, F. Gazeau, T. Pellegrino, Thermoresponsive Iron Oxide Nanocubes for an Effective Clinical Translation of Magnetic Hyperthermia and Heat-Mediated Chemotherapy, ACS Applied Materials & Interfaces 11(6) (2019) 5727-5739.

[5] S. Kralj, T. Potrc, P. Kocbek, S. Marchesan, D. Makovec, Design and fabrication of magnetically responsive nanocarriers for drug delivery, Current medicinal chemistry 24(5) (2017) 454-469.

[6] J.K. Wychowaniec, M. Iliut, B. Borek, C. Muryn, O.O. Mykhaylyk, S. Edmondson, A. Vijayaraghavan, Elastic flow instabilities and macroscopic textures in graphene oxide lyotropic liquid crystals, npj 2D Materials and Applications 5(1) (2021) 11.

[7] N. Liu, A. Chortos, T. Lei, L. Jin, T.R. Kim, W.-G. Bae, C. Zhu, S. Wang, R. Pfattner, X. Chen, R. Sinclair, Z. Bao, Ultratransparent and stretchable graphene electrodes, Science Advances 3(9) (2017).

[8] S. Sasha, A.D. Dmitriy, H.B.D. Geoffrey, M.K. Kevin, J.Z. Eric, A.S. Eric, D.P. Richard, T.N. Sonbinh, S.R. Rodney, Graphene-based composite materials, Nature 442(7100) (2006) 282.

[9] J.K. Wychowaniec, J. Litowczenko, K. Tadyszak, Fabricating versatile cell supports from nano- and micro-sized graphene oxide flakes, Journal of the Mechanical Behavior of Biomedical Materials (2019) 103594.

[10] K. Tadyszak, J.K. Wychowaniec, J. Litowczenko, Biomedical Applications of Graphene-Based Structures, Nanomaterials 8(11) (2018).

[11] J.K. Wychowaniec, M. Iliut, M. Zhou, J. Moffat, M.A. Elsawy, W.A. Pinheiro, J.A. Hoyland, A.F. Miller, A. Vijayaraghavan, A. Saiani, Designing Peptide/Graphene Hybrid Hydrogels through Fine-Tuning of Molecular Interactions, Biomacromolecules 19(7) (2018) 2731.

[12] H. Le Ferrand, S. Bolisetty, A.F. Demirors, R. Libanori, A.R. Studart, R. Mezzenga, Magnetic assembly of transparent and conducting graphene-based functional composites, Nature Communications 7 (2016).

[13] L. Wu, M. Ohtani, M. Takata, A. Saeki, S. Seki, Y. Ishida, T. Aida, Magnetically Induced Anisotropic Orientation of Graphene Oxide Locked by in Situ Hydrogelation, ACS Nano 8(5) (2014) 4640-4649.

[14] C. Yang, Z. Liu, C. Chen, K. Shi, L. Zhang, X.-J. Ju, W. Wang, R. Xie, L.-Y. Chu, Reduced Graphene Oxide-Containing Smart Hydrogels with Excellent Electro-Response and Mechanical Properties for Soft Actuators, ACS Applied Materials & Interfaces 9(18) (2017) 15758-15767.

[15] S. Mourdikoudis, A. Kostopoulou, A.P. LaGrow, Magnetic Nanoparticle Composites: Synergistic Effects and Applications, Advanced Science 8(12) (2021) 2004951.

[16] B. Shriky, A. Kelly, M. Isreb, M. Babenko, N. Mahmoudi, S. Rogers, O. Shebanova, T. Snow, T. Gough, Pluronic F127 thermosensitive injectable smart hydrogels for controlled

drug delivery system development, Journal of Colloid and Interface Science 565 (2020) 119-130.

[17] M. Bohorquez, C. Koch, T. Trygstad, N. Pandit, A Study of the Temperature-Dependent Micellization of Pluronic F127, Journal of Colloid and Interface Science 216(1) (1999) 34-40.

[18] N. Pandit, T. Trygstad, S. Croy, M. Bohorquez, C. Koch, Effect of Salts on the Micellization, Clouding, and Solubilization Behavior of Pluronic F127 Solutions, Journal of Colloid and Interface Science 222(2) (2000) 213-220.

[19] S.F. Khattak, S.R. Bhatia, S.C. Roberts, Pluronic F127 as a Cell Encapsulation Material: Utilization of Membrane-Stabilizing Agents, Tissue Engineering 11(5-6) (2005) 974-983.

[20] S.-Z. Zu, B.-H. Han, Aqueous Dispersion of Graphene Sheets Stabilized by Pluronic Copolymers: Formation of Supramolecular Hydrogel, The Journal of Physical Chemistry C 113(31) (2009) 13651-13657.

[21] A. Sahu, W.I. Choi, G. Tae, A stimuli-sensitive injectable graphene oxide composite hydrogel, Chemical Communications 48(47) (2012) 5820-5822.

[22] H. Hu, J. Yu, Y. Li, J. Zhao, H. Dong, Engineering of a novel pluronic F127/graphene nanohybrid for pH responsive drug delivery, Journal of Biomedical Materials Research Part A 100A(1) (2012) 141-148.

[23] Y. Li, J. Liu, H. Dong, G. Liu, H. Hu, Engineering of a Pluronic F127 functionalized magnetite/graphene nanohybrid for chemophototherapy, Nanotechnology 25(6) (2014) 065602.

[24] P. Monks, J.K. Wychowaniec, E. McKiernan, S. Clerkin, J. Crean, B.J. Rodriguez, E.G. Reynaud, A. Heise, D.F. Brougham, Spatiotemporally Resolved Heat Dissipation in 3D Patterned Magnetically Responsive Hydrogels, Small n/a(n/a) (2020) 2004452.

[25] A. Nuria, P. Alejandro Criado and Maurizio, Recent Advances of Graphene-based Hybrids with Magnetic Nanoparticles for Biomedical Applications, Current Medicinal Chemistry 24(5) (2017) 529-536.

[26] X. Zhu, H. Zhang, H. Huang, Y. Zhang, L. Hou, Z. Zhang, Functionalized graphene oxide-based thermosensitive hydrogel for magnetic hyperthermia therapy on tumors, Nanotechnology 26(36) (2015) 365103.

[27] L. Lartigue, P. Hugounenq, D. Alloyeau, S.P. Clarke, M. Lévy, J.-C. Bacri, R. Bazzi, D.F. Brougham, C. Wilhelm, F. Gazeau, Cooperative Organization in Iron Oxide Multi-Core Nanoparticles Potentiates Their Efficiency as Heating Mediators and MRI Contrast Agents, ACS Nano 6(12) (2012) 10935-10949.

[28] R.R. Wildeboer, P. Southern, Q.A. Pankhurst, On the reliable measurement of specific absorption rates and intrinsic loss parameters in magnetic hyperthermia materials, Journal of Physics D: Applied Physics 47(49) (2014) 495003.

[29] M. Avolio, A. Guerrini, F. Brero, C. Innocenti, C. Sangregorio, M. Cobianchi, M. Mariani, F. Orsini, P. Arosio, A. Lascialfari, In-gel study of the effect of magnetic nanoparticles immobilization on their heating efficiency for application in Magnetic Fluid Hyperthermia, Journal of Magnetism and Magnetic Materials 471 (2019) 504-512.

[30] S. van Berkum, P.D. Biewenga, S.P. Verkleij, J.B.A. van Zon, K.W.M. Boere, A. Pal, A.P. Philipse, B.H. Erné, Swelling Enhanced Remanent Magnetization of Hydrogels Cross-Linked with Magnetic Nanoparticles, Langmuir 31(1) (2015) 442-450.

[31] P. Bender, J. Fock, C. Frandsen, M.F. Hansen, C. Balceris, F. Ludwig, O. Posth, E. Wetterskog, L.K. Bogart, P. Southern, W. Szczerba, L. Zeng, K. Witte, C. Grüttner, F. Westphal, D. Honecker, D. González-Alonso, L. Fernández Barquín, C. Johansson, Relating Magnetic Properties and High Hyperthermia Performance of Iron Oxide Nanoflowers, The Journal of Physical Chemistry C 122(5) (2018) 3068-3077.

[32] P. Hugounenq, M. Levy, D. Alloyeau, L. Lartigue, E. Dubois, V. Cabuil, C. Ricolleau, S. Roux, C. Wilhelm, F. Gazeau, R. Bazzi, Iron Oxide Monocrystalline Nanoflowers for Highly Efficient Magnetic Hyperthermia, The Journal of Physical Chemistry C 116(29) (2012) 15702-15712.

[33] A.R. Studart, E. Amstad, L.J. Gauckler, Colloidal Stabilization of Nanoparticles in Concentrated Suspensions, Langmuir 23(3) (2007) 1081-1090.

[34] W.S. Hummers, R.E. Offeman, PREPARATION OF GRAPHITIC OXIDE, Journal of the American Chemical Society 80(6) (1958) 1339-1339.

[35] B. Konkena, S. Vasudevan, Understanding Aqueous Dispersibility of Graphene Oxide and Reduced Graphene Oxide through pKa Measurements, The Journal of Physical Chemistry Letters 3(7) (2012) 867-872.

[36] N.T.K. Thanh, N. Maclean, S. Mahiddine, Mechanisms of Nucleation and Growth of Nanoparticles in Solution, Chemical Reviews 114(15) (2014) 7610-7630.

[37] E.C. Vreeland, J. Watt, G.B. Schober, B.G. Hance, M.J. Austin, A.D. Price, B.D. Fellows, T.C. Monson, N.S. Hudak, L. Maldonado-Camargo, A.C. Bohorquez, C. Rinaldi, D.L. Huber, Enhanced Nanoparticle Size Control by Extending LaMer’s Mechanism, Chemistry of Materials 27(17) (2015) 6059-6066.

[38] H. Vovusha, S. Sanyal, B. Sanyal, Interaction of Nucleobases and Aromatic Amino Acids with Graphene Oxide and Graphene Flakes, The Journal of Physical Chemistry Letters 4(21) (2013) 3710-3718.

[39] A.-T. Le, C.D. Giang, L.T. Tam, T.Q. Tuan, V.N. Phan, J. Alonso, J. Devkota, E. Garaio, J.Á. García, R. Martín-Rodríguez, M.L. Fdez-Gubieda, H. Srikanth, M.-H. Phan, Enhanced magnetic anisotropy and heating efficiency in multi-functional manganese ferrite/graphene oxide nanostructures, Nanotechnology 27(15) (2016) 155707.

[40] Z. Li, Y. Li, C. Chen, Y. Cheng, Magnetic-responsive hydrogels: From strategic design to biomedical applications, Journal of Controlled Release 335 (2021) 541-556.

[41] J. Liao, H. Huang, Review on Magnetic Natural Polymer Constructed Hydrogels as Vehicles for Drug Delivery, Biomacromolecules (2020).

[42] M. Mrukiewicz, K. Kowiorski, P. Perkowski, R. Mazur, M. Djas, Threshold voltage decrease in a thermotropic nematic liquid crystal doped with graphene oxide flakes, Beilstein journal of nanotechnology 10(1) (2019) 71-78.

[43] B. Nasiłowska, Z. Bogdanowicz, K. Hińcza, Z. Mierczyk, S. Góźdź, M. Djas, K. Kowiorski, A. Bombalska, A. Kowalik, Graphene Oxide Aerosol Deposition and its Influence on Cancer Cells. Preliminary Results, Materials 13(19) (2020).

[44] D. Caruntu, G. Caruntu, Y. Chen, C.J. O'Connor, G. Goloverda, V.L. Kolesnichenko, Synthesis of Variable-Sized Nanocrystals of Fe3O4 with High Surface Reactivity, Chemistry of Materials 16(25) (2004) 5527-5534.

Graphene oxide modulates inter-particle interactions in 3D printable soft nanocomposite hydrogels restoring magnetic hyperthermia responses

– Supporting Information

Esther Rani Aluri[a], Edward Gannon[a], Krutika Singh[a], Srikanth Kolagatla[b,c], Krystian Kowiorski[d], Sameer Shingte[a], Eoin M^{c}Kiernan[a], Cara Moloney[a], Katie M^{c}Garry[a], Liam Jowett[a], Brian J. Rodriguez[b,c], Dermot F. Brougham[a,]*, Jacek K. Wychowaniec[a,1,]*

[a]School of Chemistry, University College Dublin, Belfield, Dublin 4, Ireland

[b]Conway Institute of Biomolecular and Biomedical Research, University College Dublin, Belfield, Dublin 4, Ireland

[c]School of Physics, University College Dublin, Belfield, Dublin 4, Ireland

[d]Łukasiewicz Research Network - Institute of Microelectronics and Photonics, Research group - Functional Materials, Lotników 32/46, 02-668 Warsaw

[1] Current address:

AO Research Institute Davos, Clavadelerstrasse 8, 7270, Davos, Switzerland

e-mail: jacek.wychowaniec@aofoundation.org

* Corresponding authors:

J.K.W. Phone: (+353)0899724612;

e-mails: jacek.wychowaniec@ucd.ie; jacek.wychowaniec@aofoundation.org

D.F.B. Phone: (+353)017162077;

e-mail: dermot.brougham@ucd.ie

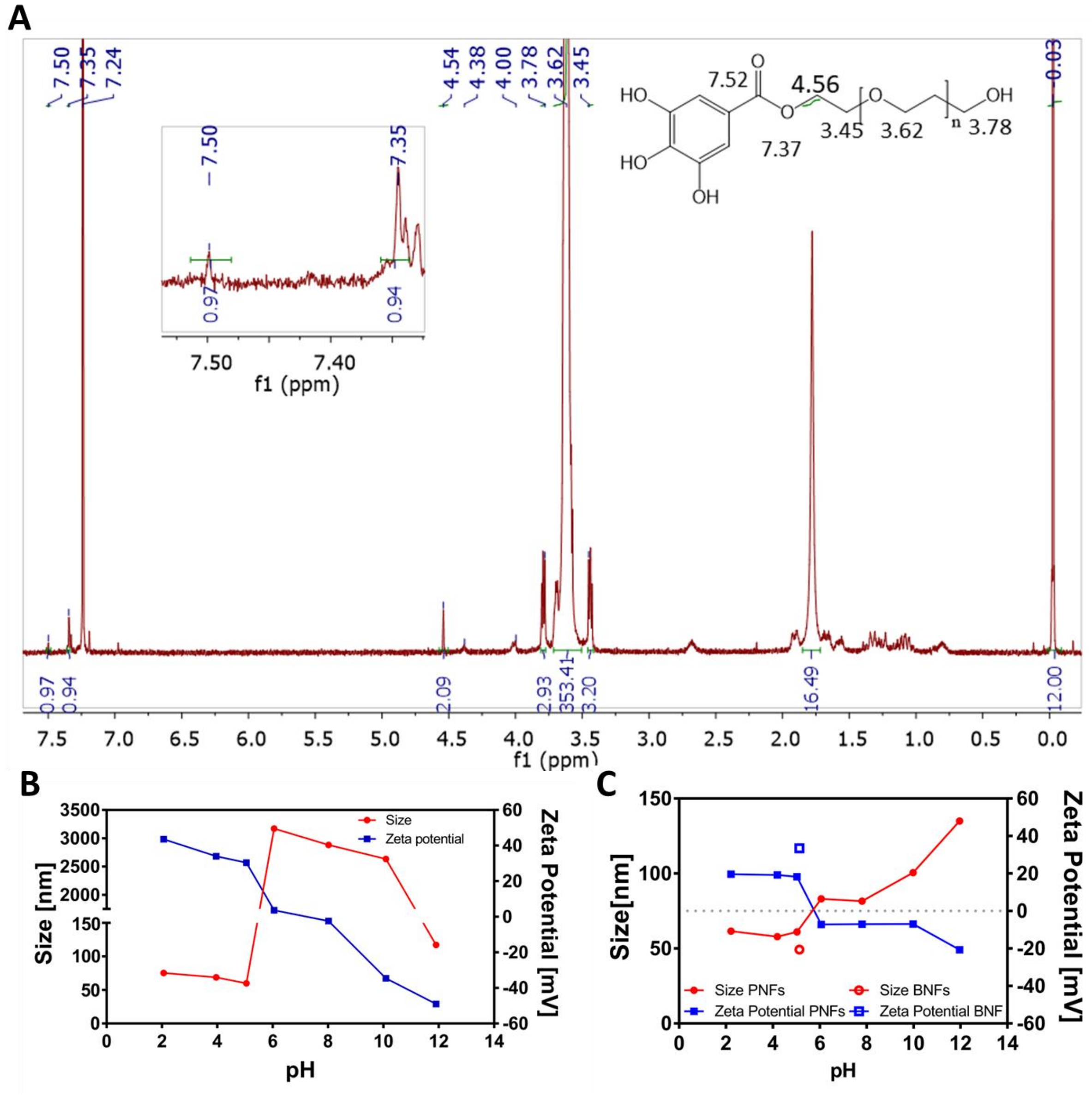

***Figure S1**. Characterization of BNFs and PNFs. **(A)** ^{1}H NMR spectrum of PEG8000-Gallol. ^{1}H NMR (500 MHz, CDCl$_3$) δ_{ppm}: 3.78 (triplet, backbone-$\mathbf{CH}_2$ OH), 3.45 (triplet, $\mathbf{CH}_2$-CH$_2$OC(=O)), 3.62 (multiplet, C$\mathbf{H}_2$C$\mathbf{H}_2$O PEG backbone), 4.56 (2H, C$\mathbf{H}_2$OC(=O)), 7.35-7.50 (Aromatic proton peaks). Obtained peaks match those obtained in the same PEG-Gallol synthesis described by [1]. **(B)** pH dependence of the size (red plots) and zeta potential (ζ_p) (blue plots) for the BNFs. **(C)** pH dependence of the size (red plots) and zeta potential (ζ_p) (blue plots) for the PNFs. BNFs size (red open circle) and ζ_p (blue open square) are also reported for comparison. Fe concentration (0.025 mg mL^{-1}) and PEG-Gallol concentration (0.044 mg mL^{-1}) were kept constant throughout. In a separate experiment we noted that 0.044 mg mL^{-1} (x 1.75 mass ratio) was the minimum sufficient PEG-Gallol concentration leading to full coverage of BNFs, to provide full stability across all pH values.*

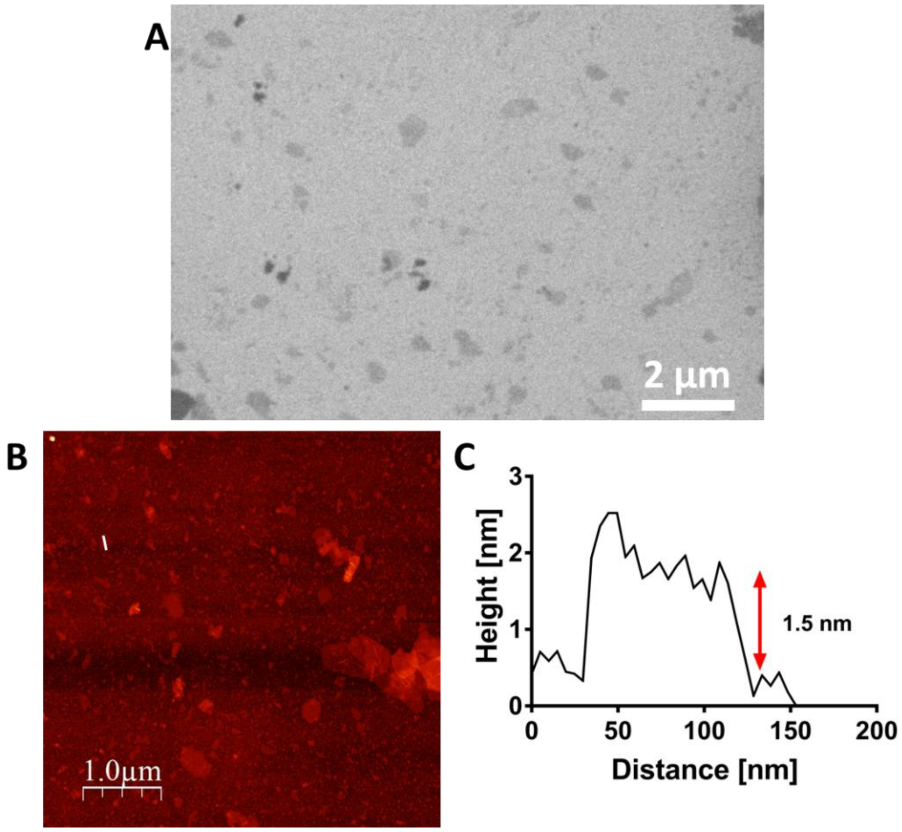

Figure S2. *Characterization of graphene oxide (GO) flakes.* ***(A)*** *SEM and* ***(B)*** *AFM images of GO flakes.* ***(C)*** *AFM micrograph of GO showing step height profile of the individual flake depicted by the white line in* ***(B)****.*

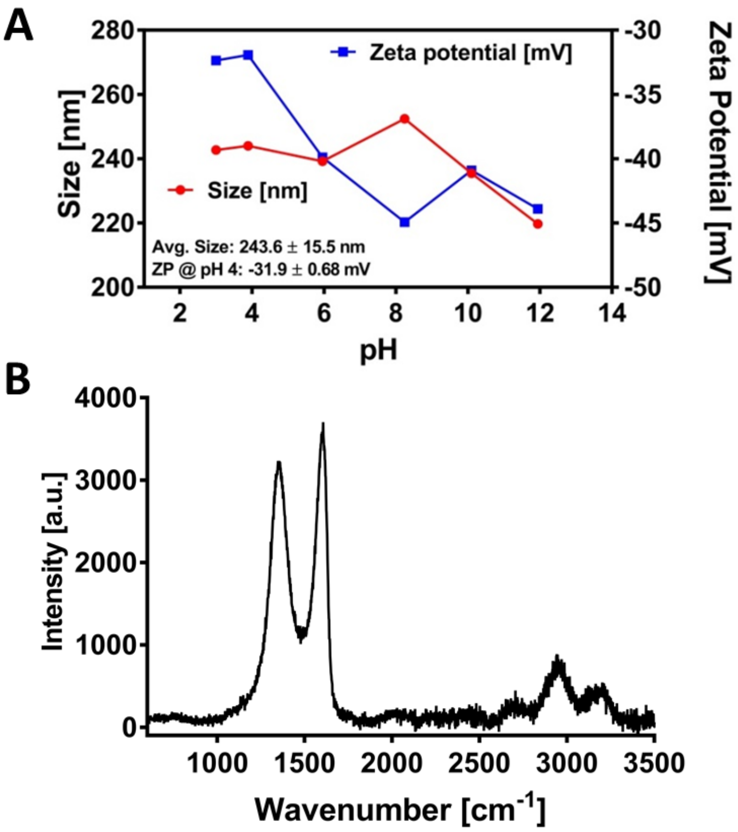

Figure S3. *Characterization of graphene oxide (GO) flakes.* ***(A)*** *pH dependence of the hydrodynamic size (●) and* ζ_p *(■) of GO. The average size depicted in Figure is taken as an average of the* d_{hyd} *values obtained at each pH.* ***(B)*** *Raman spectroscopy of GO showing the typical D (1354 cm*$^{-1}$*) and G (1596 cm*$^{-1}$*) bands with the obtained ratio of the two peaks:* $I_D/I_G=1.15$.

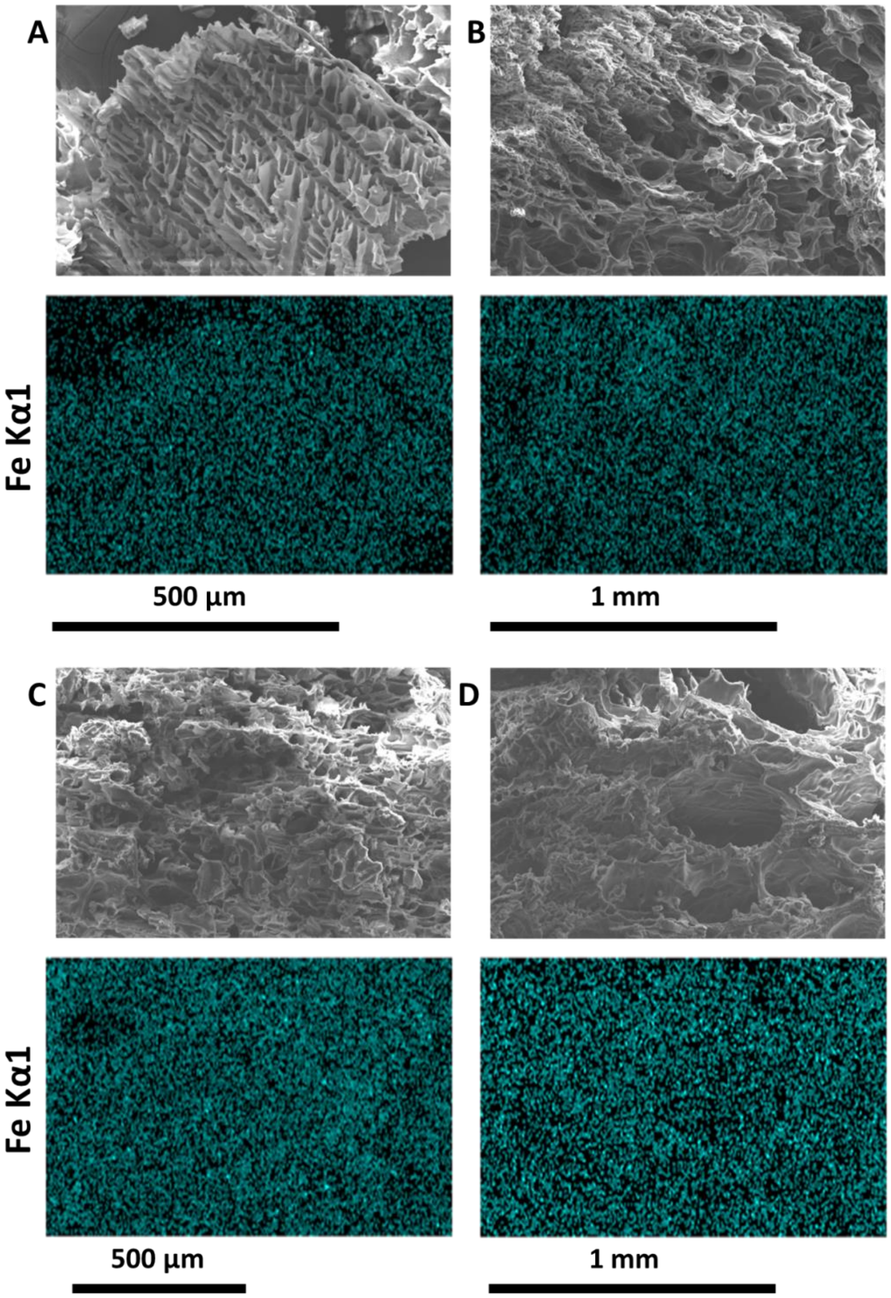

Figure S4. *Scanning electron microscopy with associated Fe distribution maps of;* ***(A)*** *gPNF;* ***(B)*** *gPNF_0.3GO;* ***(C)*** *gPNF_0.5GO;* ***(D)*** *gPNF_1.08GO a concentration of Fe ~2.70 ± 0.3 mg mL*$^{-1}$*. In all cases similar Fe composition, of between 0.1-0.3 At%, was obtained.*

Table S1. *SAR values as a function of probe depth for 2.3 mg mL^{-1} Fe – 0.5 mg mL^{-1} GO sPNF_GO and gPNF_GO.*

Sample:	**sPNF_GO** **2.3 mg mL^{-1} Fe** **0.5 mg mL^{-1} GO**	**gPNF_GO** **2.3 mg mL^{-1} Fe** **0.5 mg mL^{-1} GO**
Depth[1] [mm]	**SAR [W.g^{-1}]**	
20	184	111
15	203	118
10	194	115
5	203	112

1. *Defined as depth from the upper surface of the 20 mm deep (1 mL) samples.*

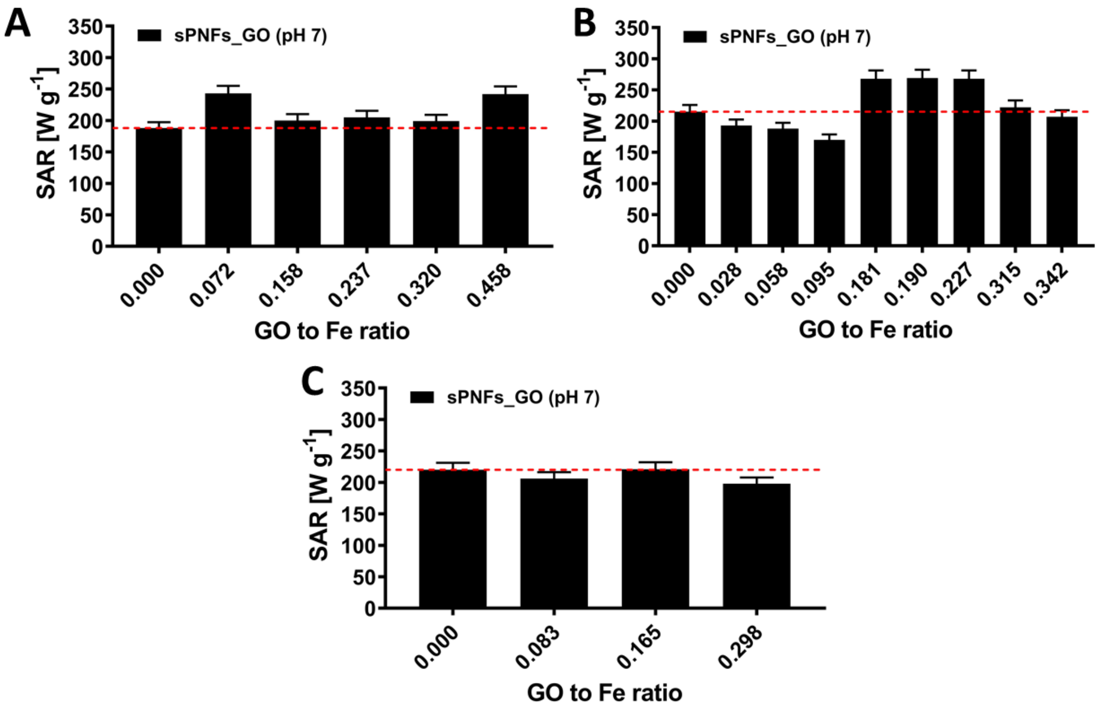

Figure S5. *SAR values (see Equation 1, main article) for three independent NFs batches* ***(A)-(C)*** *of sPNF_GO as a function of GO concentration, represented as GO to Fe ratio, at pH 7, (at (A) Fe ~2.6 ± 0.2 , (B) 2.9 ± 0.4, (C) 3.6 ± 0.4 mg mL^{-1} Fe) The horizontal dashed lines in all panels indicate the native SAR values of the corresponding sPNF suspensions (without any GO). Error bar estimations are described in Methods.*

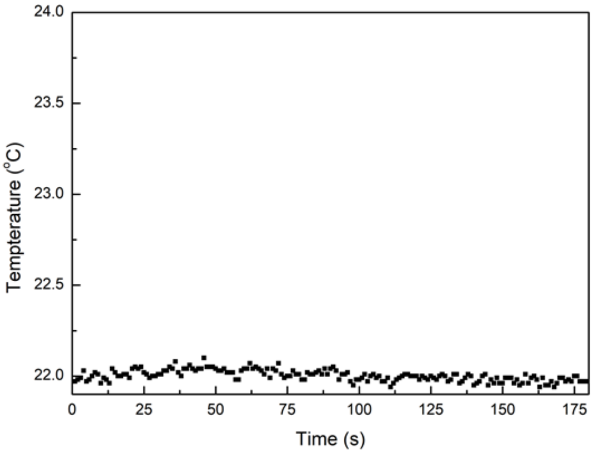

Figure S6. *Hyperthermic response of GO flakes at 0.6 mg mL^{-1} and pH 4 over 180 seconds, determined at ν_{AC}=535 kHz, I_{AC}=24 mT. Lack of any significant heating response is evident.*

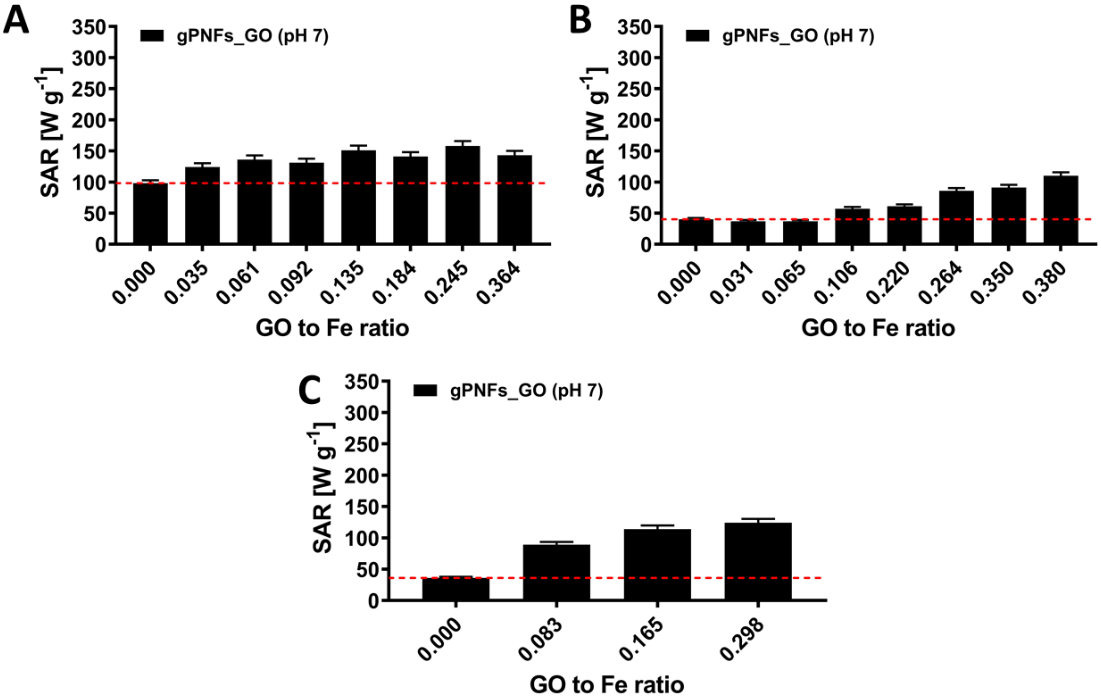

Figure S7. *SAR values (see Equation 1, main article) for three independent NFs batches* ***(A)-(C)*** *of gPNF_GO as a function of GO concentration, represented as GO to Fe ratio, at pH 7, (at (A) Fe ~2.5 ± 0.2, (B) 2.7 ±0.4, (C) 3.6 ± 0.4 mg mL^{-1} Fe). All graphs have the same Y axis for ease of comparison. The horizontal dashed lines in all panels indicate the SAR values* *of the corresponding gPNF samples (hydrogels without any GO). Error bar estimations are described in Methods.*

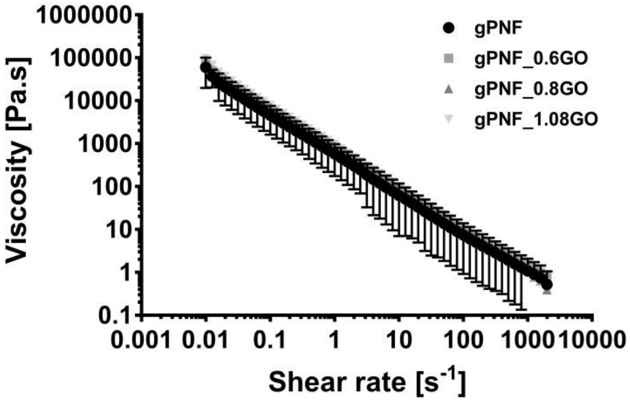

Figure S8. *Viscosity versus shear rate curve of all printed gPNF_GO nanocomposite gels presented in* ***Figure 5****, taken at 19°C. Average of two runs and standard deviation are presented.*

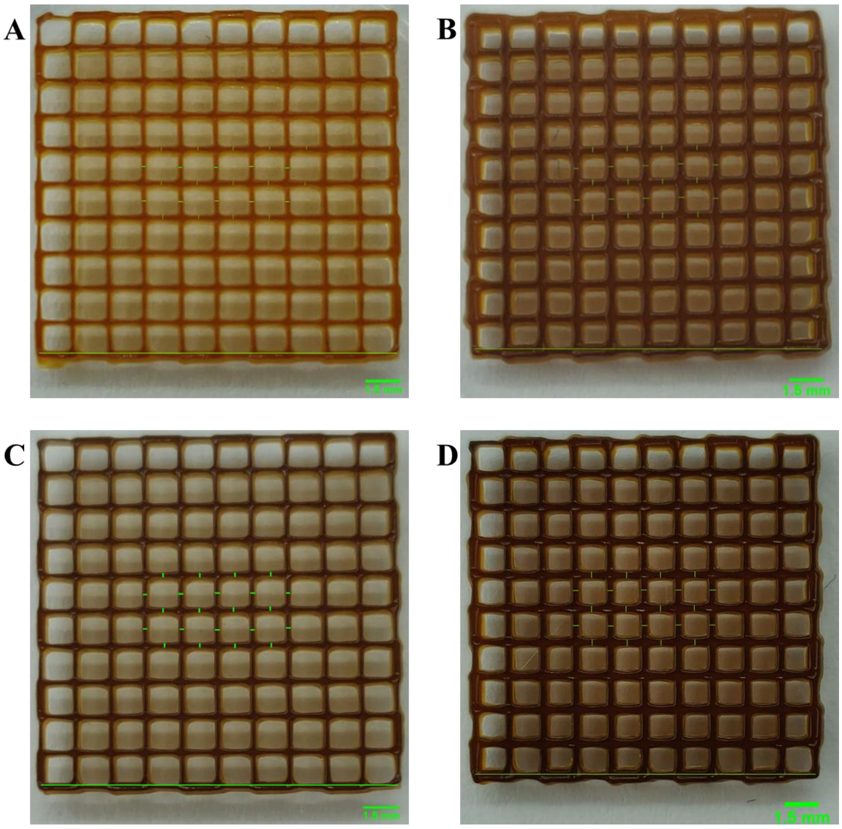

Figure S9. *Measurements of grid thicknesses from optical images for* ***(A)*** *gPNF_0GO,* ***(B)*** *gPNF_0.6GO.* ***(C)*** *gPNF_0.8GO and* ***(D)*** *gPNF_1.08GO.*

Table S2. *Gcodes used for printing grids gPNF_0.0GO, gPNF_0.6GO, gPNF_0.8GO, and gPNF_1.08GO.*

0.0 GO	0.6 GO	0.8, 1.08 GO
M104 S200 ; set temperature	M104 S200 ; set temperature	M104 S200 ; set temperature
G28 ; home all axes	G28 ; home all axes	G28 ; home all axes
; Filament gcode	; Filament gcode	; Filament gcode
; set up	; set up	; set up
M109 S200 ; set temperature and wait for it to be reached	M109 S200 ; set temperature and wait for it to be reached	M109 S200 ; set temperature and wait for it to be reached
G21 ; set units to millimeters	G21 ; set units to millimeters	G21 ; set units to millimeters
M82 ; use absolute distances for extrusion	M82 ; use absolute distances for extrusion	M82 ; use absolute distances for extrusion
G92 E0	G92 E0	G92 E0
G1 F300;	G1 F200;	G1 F200;
G1 X15 E1	G1 X15 E1	G1 X15 E1
G1 Y15 E1.2	G1 Y15 E1.2	G1 Y15 E1.2
G1 X0 E1.3	G1 X0 E1.3	G1 X0 E1.3
G1 Y0 E1.4	G1 Y0 E1.4	G1 Y0 E1.4
G1 X1.5 E0	G1 X1.5 E0	G1 X1.5 E0
G1 Y15 E1.6	G1 Y15 E1.6	G1 Y15 E1.6
G1 X3 E0	G1 X3 E0	G1 X3 E0
G1 Y0 E1.8	G1 Y0 E1.8	G1 Y0 E1.8
G1 X4.5 E0	G1 X4.5 E0	G1 X4.5 E0
G1 Y15 E1.9	G1 Y15 E1.9	G1 Y15 E1.9
G1 X6 E0	G1 X6 E0	G1 X6 E0
G1 Y0 E1.97	G1 Y0 E1.97	G1 Y0 E1.97
G1 X7.5 E0	G1 X7.5 E0	G1 X7.5 E0
G1 Y15 E1.2	G1 Y15 E1.2	G1 Y15 E1.2
G1 X9 E0	G1 X9 E0	G1 X9 E0
G1 Y0 E1.4	G1 Y0 E1.4	G1 Y0 E1.4
G1 X10.5 E0	G1 X10.5 E0	G1 X10.5 E0
G1 Y15 E1.6	G1 Y15 E1.6	G1 Y15 E1.6
G1 X12 E0	G1 X12 E0	G1 X12 E0
G1 Y0 E1.8	G1 Y0 E1.8	G1 Y0 E1.8
G1 X13.5 E0	G1 X13.5 E0	G1 X13.5 E0
G1 Y15 E1.9	G1 Y15 E1.9	G1 Y15 E1.9
G1 X15 Y15 E0	G1 X15 Y15 E0	G1 X15 Y15 E0
G1 Y13.5 E1.91	G1 Y13.5 E1.91	G1 Y13.5 E1.91
G1 X0 E1.92	G1 X0 E1.92	G1 X0 E1.92

G1 Y12 E0	G1 Y12 E0	G1 Y12 E0
G1 X15 E1.95	G1 X15 E1.95	G1 X15 E1.95
G1 Y10.5 E0	G1 Y10.5 E0	G1 Y10.5 E0
G1 X0 E1	G1 X0 E1	G1 X0 E1
G1 Y9 E0	G1 Y9 E0	G1 Y9 E0
G1 X15 E1.3	G1 X15 E1.3	G1 X15 E1.3
G1 Y7.5 E0	G1 Y7.5 E0	G1 Y7.5 E0
G1 X0 E1.4	G1 X0 E1.4	G1 X0 E1.4
G1 Y6 E0	G1 Y6 E0	G1 Y6 E0
G1 X15 E1	G1 X15 E1	G1 X15 E1
G1 Y4.5 E0	G1 Y4.5 E0	G1 Y4.5 E0
G1 X0 E1	G1 X0 E1	G1 X0 E1
G1 Y3 E0	G1 Y3 E0	G1 Y3 E0
G1 X15 E1.6	G1 X15 E1.6	G1 X15 E1.6
G1 Y1.5 E0	G1 Y1.5 E0	G1 Y1.5 E0
G1 X0 E1.8	G1 X0 E1.8	G1 X0 E1.8
G1 Y0 E0	G1 Y0 E0	G1 Y0 E0
G0 Z0.08 E0	G0 Z0.08 E0	G0 Z0.08 E0
;LAYER 1	;LAYER 1	;LAYER 1
G1 X15 E1	G1 F200 X15 E1	G1 X15 E1
G1 Y15 E1.2	G1 Y15 E1.2	G1 Y15 E1.2
G1 X0 E1.3	G1 X0 E1.3	G1 X0 E1.3
G1 Y0 E1.4	G1 Y0 E1.4	G1 Y0 E1.4
G1 X1.5 E0	G1 F300 X1.5 E0	G1 X1.5 E0
G1 Y15 E1.6	G1 Y15 E1.6	G1 Y15 E1.6
G1 X3 E0	G1 X3 E0	G1 X3 E0
G1 Y0 E1.8	G1 Y0 E1.8	G1 Y0 E1.8
G1 X4.5 E0	G1 X4.5 E0	G1 X4.5 E0
G1 Y15 E1.9	G1 Y15 E1.9	G1 Y15 E1.9
G1 X6 E0	G1 X6 E0	G1 X6 E0
G1 Y0 E1.97	G1 Y0 E1.97	G1 Y0 E1.97
G1 X7.5 E0	G1 X7.5 E0	G1 X7.5 E0
G1 Y15 E1.2	G1 Y15 E1.2	G1 Y15 E1.2
G1 X9 E0	G1 X9 E0	G1 X9 E0
G1 Y0 E1.4	G1 Y0 E1.4	G1 Y0 E1.4
G1 X10.5 E0	G1 X10.5 E0	G1 X10.5 E0
G1 Y15 E1.6	G1 Y15 E1.6	G1 Y15 E1.6
G1 X12 E0	G1 X12 E0	G1 X12 E0
G1 Y0 E1.8	G1 Y0 E1.8	G1 Y0 E1.8
G1 X13.5 E0	G1 X13.5 E0	G1 X13.5 E0
G1 Y15 E1.9	G1 Y15 E1.9	G1 Y15 E1.9
G1 X15 Y15 E0	G1 X15 Y15 E0	G1 X15 Y15 E0
G1 Y13.5 E1.91	G1 Y13.5 E1.91	G1 Y13.5 E1.91
G1 X0 E1.92	G1 X0 E1.92	G1 X0 E1.92
G1 Y12 E0	G1 Y12 E0	G1 Y12 E0
G1 X15 E1.95	G1 X15 E1.95	G1 X15 E1.95

G1 Y10.5 E0	G1 Y10.5 E0	G1 Y10.5 E0
G1 X0 E1	G1 X0 E1	G1 X0 E1
G1 Y9 E0	G1 Y9 E0	G1 Y9 E0
G1 X15 E1.3	G1 X15 E1.3	G1 X15 E1.3
G1 Y7.5 E0	G1 Y7.5 E0	G1 Y7.5 E0
G1 X0 E1.4	G1 X0 E1.4	G1 X0 E1.4
G1 Y6 E0	G1 Y6 E0	G1 Y6 E0
G1 X15 E1	G1 X15 E1	G1 X15 E1
G1 Y4.5 E0	G1 Y4.5 E0	G1 Y4.5 E0
G1 X0 E1	G1 X0 E1	G1 X0 E1
G1 Y3 E0	G1 Y3 E0	G1 Y3 E0
G1 X15 E1.6	G1 X15 E1.6	G1 X15 E1.6
G1 Y1.5 E0	G1 Y1.5 E0	G1 Y1.5 E0
G1 X0 E1.8	G1 X0 E1.8	G1 X0 E1.8
G1 Y0 E0	G1 Y0 E0	G1 Y0 E0
G0 Z0.17 E0	G0 Z0.17 E0	G0 Z0.17 E0
;LAYER 2	;LAYER 2	;LAYER 2
G1 X15 E1	G1 F200 X15 E1	G1 X15 E1
G1 Y15 E1.2	G1 Y15 E1.2	G1 Y15 E1.2
G1 X0 E1.3	G1 X0 E1.3	G1 X0 E1.3
G1 Y0 E1.4	G1 Y0 E1.4	G1 Y0 E1.4
G1 X1.5 E0	G1 F300 X1.5 E0	G1 X1.5 E0
G1 Y15 E1.6	G1 Y15 E1.6	G1 Y15 E1.6
G1 X3 E0	G1 X3 E0	G1 X3 E0
G1 Y0 E1.8	G1 Y0 E1.8	G1 Y0 E1.8
G1 X4.5 E0	G1 X4.5 E0	G1 X4.5 E0
G1 Y15 E1.9	G1 Y15 E1.9	G1 Y15 E1.9
G1 X6 E0	G1 X6 E0	G1 X6 E0
G1 Y0 E1.97	G1 Y0 E1.97	G1 Y0 E1.97
G1 X7.5 E0	G1 X7.5 E0	G1 X7.5 E0
G1 Y15 E1.2	G1 Y15 E1.2	G1 Y15 E1.2
G1 X9 E0	G1 X9 E0	G1 X9 E0
G1 Y0 E1.4	G1 Y0 E1.4	G1 Y0 E1.4
G1 X10.5 E0	G1 X10.5 E0	G1 X10.5 E0
G1 Y15 E1.6	G1 Y15 E1.6	G1 Y15 E1.6
G1 X12 E0	G1 X12 E0	G1 X12 E0
G1 Y0 E1.8	G1 Y0 E1.8	G1 Y0 E1.8
G1 X13.5 E0	G1 X13.5 E0	G1 X13.5 E0
G1 Y15 E1.9	G1 Y15 E1.9	G1 Y15 E1.9
G1 X15 Y15 E0	G1 X15 Y15 E0	G1 X15 Y15 E0
G1 Y13.5 E1.91	G1 Y13.5 E1.91	G1 Y13.5 E1.91
G1 X0 E1.92	G1 X0 E1.92	G1 X0 E1.92
G1 Y12 E0	G1 Y12 E0	G1 Y12 E0
G1 X15 E1.95	G1 X15 E1.95	G1 X15 E1.95
G1 Y10.5 E0	G1 Y10.5 E0	G1 Y10.5 E0
G1 X0 E1	G1 X0 E1	G1 X0 E1

G1 Y9 E0	G1 Y9 E0	G1 Y9 E0
G1 X15 E1.3	G1 X15 E1.3	G1 X15 E1.3
G1 Y7.5 E0	G1 Y7.5 E0	G1 Y7.5 E0
G1 X0 E1.4	G1 X0 E1.4	G1 X0 E1.4
G1 Y6 E0	G1 Y6 E0	G1 Y6 E0
G1 X15 E1	G1 X15 E1	G1 X15 E1
G1 Y4.5 E0	G1 Y4.5 E0	G1 Y4.5 E0
G1 X0 E1	G1 X0 E1	G1 X0 E1
G1 Y3 E0	G1 Y3 E0	G1 Y3 E0
G1 X15 E1.6	G1 X15 E1.6	G1 X15 E1.6
G1 Y1.5 E0	G1 Y1.5 E0	G1 Y1.5 E0
G1 X0 E1.8	G1 X0 E1.8	G1 X0 E1.8
G1 Y0 E0	G1 Y0 E0	G1 Y0 E0
G0 Z0.25 E0	G0 Z0.25 E0	G0 Z0.25 E0
;LAYER 3	;LAYER 3	;LAYER 3
G1 X15 E1	G1 F200 X15 E1	G1 X15 E1
G1 Y15 E1.2	G1 Y15 E1.2	G1 Y15 E1.2
G1 X0 E1.3	G1 X0 E1.3	G1 X0 E1.3
G1 Y0 E1.4	G1 Y0 E1.4	G1 Y0 E1.4
G1 X1.5 E0	G1 F300 X1.5 E0	G1 X1.5 E0
G1 Y15 E1.6	G1 Y15 E1.6	G1 Y15 E1.6
G1 X3 E0	G1 X3 E0	G1 X3 E0
G1 Y0 E1.8	G1 Y0 E1.8	G1 Y0 E1.8
G1 X4.5 E0	G1 X4.5 E0	G1 X4.5 E0
G1 Y15 E1.9	G1 Y15 E1.9	G1 Y15 E1.9
G1 X6 E0	G1 X6 E0	G1 X6 E0
G1 Y0 E1.97	G1 Y0 E1.97	G1 Y0 E1.97
G1 X7.5 E0	G1 X7.5 E0	G1 X7.5 E0
G1 Y15 E1.2	G1 Y15 E1.2	G1 Y15 E1.2
G1 X9 E0	G1 X9 E0	G1 X9 E0
G1 Y0 E1.4	G1 Y0 E1.4	G1 Y0 E1.4
G1 X10.5 E0	G1 X10.5 E0	G1 X10.5 E0
G1 Y15 E1.6	G1 Y15 E1.6	G1 Y15 E1.6
G1 X12 E0	G1 X12 E0	G1 X12 E0
G1 Y0 E1.8	G1 Y0 E1.8	G1 Y0 E1.8
G1 X13.5 E0	G1 X13.5 E0	G1 X13.5 E0
G1 Y15 E1.9	G1 Y15 E1.9	G1 Y15 E1.9
G1 X15 Y15 E0	G1 X15 Y15 E0	G1 X15 Y15 E0
G1 Y13.5 E1.91	G1 Y13.5 E1.91	G1 Y13.5 E1.91
G1 X0 E1.92	G1 X0 E1.92	G1 X0 E1.92
G1 Y12 E0	G1 Y12 E0	G1 Y12 E0
G1 X15 E1.95	G1 X15 E1.95	G1 X15 E1.95
G1 Y10.5 E0	G1 Y10.5 E0	G1 Y10.5 E0
G1 X0 E1	G1 X0 E1	G1 X0 E1
G1 Y9 E0	G1 Y9 E0	G1 Y9 E0
G1 X15 E1.3	G1 X15 E1.3	G1 X15 E1.3

G1 Y7.5 E0	G1 Y7.5 E0	G1 Y7.5 E0
G1 X0 E1.4	G1 X0 E1.4	G1 X0 E1.4
G1 Y6 E0	G1 Y6 E0	G1 Y6 E0
G1 X15 E1	G1 X15 E1	G1 X15 E1
G1 Y4.5 E0	G1 Y4.5 E0	G1 Y4.5 E0
G1 X0 E1	G1 X0 E1	G1 X0 E1
G1 Y3 E0	G1 Y3 E0	G1 Y3 E0
G1 X15 E1.6	G1 X15 E1.6	G1 X15 E1.6
G1 Y1.5 E0	G1 Y1.5 E0	G1 Y1.5 E0
G1 X0 E1.8	G1 X0 E1.8	G1 X0 E1.8
G1 Y0 E0	G1 Y0 E0	G1 Y0 E0
G0 Z0.25 E0	G0 Z0.25 E0	G0 Z0.25 E0
;LAYER 4	;LAYER 4	;LAYER 4
G1 X15 E1	G1 F200 X15 E1	G1 X15 E1
G1 Y15 E1.2	G1 Y15 E1.2	G1 Y15 E1.2
G1 X0 E1.3	G1 X0 E1.3	G1 X0 E1.3
G1 Y0 E1.4	G1 Y0 E1.4	G1 Y0 E1.4
G1 X1.5 E0	G1 F300 X1.5 E0	G1 X1.5 E0
G1 Y15 E1.6	G1 Y15 E1.6	G1 Y15 E1.6
G1 X3 E0	G1 X3 E0	G1 X3 E0
G1 Y0 E1.8	G1 Y0 E1.8	G1 Y0 E1.8
G1 X4.5 E0	G1 X4.5 E0	G1 X4.5 E0
G1 Y15 E1.9	G1 Y15 E1.9	G1 Y15 E1.9
G1 X6 E0	G1 X6 E0	G1 X6 E0
G1 Y0 E1.97	G1 Y0 E1.97	G1 Y0 E1.97
G1 X7.5 E0	G1 X7.5 E0	G1 X7.5 E0
G1 Y15 E1.2	G1 Y15 E1.2	G1 Y15 E1.2
G1 X9 E0	G1 X9 E0	G1 X9 E0
G1 Y0 E1.4	G1 Y0 E1.4	G1 Y0 E1.4
G1 X10.5 E0	G1 X10.5 E0	G1 X10.5 E0
G1 Y15 E1.6	G1 Y15 E1.6	G1 Y15 E1.6
G1 X12 E0	G1 X12 E0	G1 X12 E0
G1 Y0 E1.8	G1 Y0 E1.8	G1 Y0 E1.8
G1 X13.5 E0	G1 X13.5 E0	G1 X13.5 E0
G1 Y15 E1.9	G1 Y15 E1.9	G1 Y15 E1.9
G1 X15 Y15 E0	G1 X15 Y15 E0	G1 X15 Y15 E0
G1 Y13.5 E1.91	G1 Y13.5 E1.91	G1 Y13.5 E1.91
G1 X0 E1.92	G1 X0 E1.92	G1 X0 E1.92
G1 Y12 E0	G1 Y12 E0	G1 Y12 E0
G1 X15 E1.95	G1 X15 E1.95	G1 X15 E1.95
G1 Y10.5 E0	G1 Y10.5 E0	G1 Y10.5 E0
G1 X0 E1	G1 X0 E1	G1 X0 E1
G1 Y9 E0	G1 Y9 E0	G1 Y9 E0
G1 X15 E1.3	G1 X15 E1.3	G1 X15 E1.3
G1 Y7.5 E0	G1 Y7.5 E0	G1 Y7.5 E0
G1 X0 E1.4	G1 X0 E1.4	G1 X0 E1.4

G1 Y6 E0	G1 Y6 E0	G1 Y6 E0
G1 X15 E1	G1 X15 E1	G1 X15 E1
G1 Y4.5 E0	G1 Y4.5 E0	G1 Y4.5 E0
G1 X0 E1	G1 X0 E1	G1 X0 E1
G1 Y3 E0	G1 Y3 E0	G1 Y3 E0
G1 X15 E1.6	G1 X15 E1.6	G1 X15 E1.6
G1 Y1.5 E0	G1 Y1.5 E0	G1 Y1.5 E0
G1 X0 E1.8	G1 X0 E1.8	G1 X0 E1.8
G1 Y0 E0	G1 Y0 E0	G1 Y0 E0
G0 Z0.33 E0	G0 Z0.33 E0	G0 Z0.33 E0
;LAYER 5	;LAYER 5	;LAYER 5
G1 X15 E1	G1 F200 X15 E1	G1 X15 E1
G1 Y15 E1.2	G1 Y15 E1.2	G1 Y15 E1.2
G1 X0 E1.3	G1 X0 E1.3	G1 X0 E1.3
G1 Y0 E1.4	G1 Y0 E1.4	G1 Y0 E1.4
G1 X1.5 E0	G1 F300 X1.5 E0	G1 X1.5 E0
G1 Y15 E1.6	G1 Y15 E1.6	G1 Y15 E1.6
G1 X3 E0	G1 X3 E0	G1 X3 E0
G1 Y0 E1.8	G1 Y0 E1.8	G1 Y0 E1.8
G1 X4.5 E0	G1 X4.5 E0	G1 X4.5 E0
G1 Y15 E1.9	G1 Y15 E1.9	G1 Y15 E1.9
G1 X6 E0	G1 X6 E0	G1 X6 E0
G1 Y0 E1.97	G1 Y0 E1.97	G1 Y0 E1.97
G1 X7.5 E0	G1 X7.5 E0	G1 X7.5 E0
G1 Y15 E1.2	G1 Y15 E1.2	G1 Y15 E1.2
G1 X9 E0	G1 X9 E0	G1 X9 E0
G1 Y0 E1.4	G1 Y0 E1.4	G1 Y0 E1.4
G1 X10.5 E0	G1 X10.5 E0	G1 X10.5 E0
G1 Y15 E1.6	G1 Y15 E1.6	G1 Y15 E1.6
G1 X12 E0	G1 X12 E0	G1 X12 E0
G1 Y0 E1.8	G1 Y0 E1.8	G1 Y0 E1.8
G1 X13.5 E0	G1 X13.5 E0	G1 X13.5 E0
G1 Y15 E1.9	G1 Y15 E1.9	G1 Y15 E1.9
G1 X15 Y15 E0	G1 X15 Y15 E0	G1 X15 Y15 E0
G1 Y13.5 E1.91	G1 Y13.5 E1.91	G1 Y13.5 E1.91
G1 X0 E1.92	G1 X0 E1.92	G1 X0 E1.92
G1 Y12 E0	G1 Y12 E0	G1 Y12 E0
G1 X15 E1.95	G1 X15 E1.95	G1 X15 E1.95
G1 Y10.5 E0	G1 Y10.5 E0	G1 Y10.5 E0
G1 X0 E1	G1 X0 E1	G1 X0 E1
G1 Y9 E0	G1 Y9 E0	G1 Y9 E0
G1 X15 E1.3	G1 X15 E1.3	G1 X15 E1.3
G1 Y7.5 E0	G1 Y7.5 E0	G1 Y7.5 E0
G1 X0 E1.4	G1 X0 E1.4	G1 X0 E1.4
G1 Y6 E0	G1 Y6 E0	G1 Y6 E0
G1 X15 E1	G1 X15 E1	G1 X15 E1

G1 Y4.5 E0	G1 Y4.5 E0	G1 Y4.5 E0
G1 X0 E1	G1 X0 E1	G1 X0 E1
G1 Y3 E0	G1 Y3 E0	G1 Y3 E0
G1 X15 E1.6	G1 X15 E1.6	G1 X15 E1.6
G1 Y1.5 E0	G1 Y1.5 E0	G1 Y1.5 E0
G1 X0 E1.8	G1 X0 E1.8	G1 X0 E1.8
G1 Y0 E0	G1 Y0 E0	G1 Y0 E0
G0 Z0.4 E0	G0 Z0.4 E0	G0 Z0.4 E0
;LAYER 6	;LAYER 6	;LAYER 6
G1 X15 E1	G1 F200 X15 E1	G1 X15 E1
G1 Y15 E1.2	G1 Y15 E1.2	G1 Y15 E1.2
G1 X0 E1.3	G1 X0 E1.3	G1 X0 E1.3
G1 Y0 E1.4	G1 Y0 E1.4	G1 Y0 E1.4
G1 X1.5 E0	G1 F300 X1.5 E0	G1 X1.5 E0
G1 Y15 E1.6	G1 Y15 E1.6	G1 Y15 E1.6
G1 X3 E0	G1 X3 E0	G1 X3 E0
G1 Y0 E1.8	G1 Y0 E1.8	G1 Y0 E1.8
G1 X4.5 E0	G1 X4.5 E0	G1 X4.5 E0
G1 Y15 E1.9	G1 Y15 E1.9	G1 Y15 E1.9
G1 X6 E0	G1 X6 E0	G1 X6 E0
G1 Y0 E1.97	G1 Y0 E1.97	G1 Y0 E1.97
G1 X7.5 E0	G1 X7.5 E0	G1 X7.5 E0
G1 Y15 E1.2	G1 Y15 E1.2	G1 Y15 E1.2
G1 X9 E0	G1 X9 E0	G1 X9 E0
G1 Y0 E1.4	G1 Y0 E1.4	G1 Y0 E1.4
G1 X10.5 E0	G1 X10.5 E0	G1 X10.5 E0
G1 Y15 E1.6	G1 Y15 E1.6	G1 Y15 E1.6
G1 X12 E0	G1 X12 E0	G1 X12 E0
G1 Y0 E1.8	G1 Y0 E1.8	G1 Y0 E1.8
G1 X13.5 E0	G1 X13.5 E0	G1 X13.5 E0
G1 Y15 E1.9	G1 Y15 E1.9	G1 Y15 E1.9
G1 X15 Y15 E0	G1 X15 Y15 E0	G1 X15 Y15 E0
G1 Y13.5 E1.91	G1 Y13.5 E1.91	G1 Y13.5 E1.91
G1 X0 E1.92	G1 X0 E1.92	G1 X0 E1.92
G1 Y12 E0	G1 Y12 E0	G1 Y12 E0
G1 X15 E1.95	G1 X15 E1.95	G1 X15 E1.95
G1 Y10.5 E0	G1 Y10.5 E0	G1 Y10.5 E0
G1 X0 E1	G1 X0 E1	G1 X0 E1
G1 Y9 E0	G1 Y9 E0	G1 Y9 E0
G1 X15 E1.3	G1 X15 E1.3	G1 X15 E1.3
G1 Y7.5 E0	G1 Y7.5 E0	G1 Y7.5 E0
G1 X0 E1.4	G1 X0 E1.4	G1 X0 E1.4
G1 Y6 E0	G1 Y6 E0	G1 Y6 E0
G1 X15 E1	G1 X15 E1	G1 X15 E1
G1 Y4.5 E0	G1 Y4.5 E0	G1 Y4.5 E0
G1 X0 E1	G1 X0 E1	G1 X0 E1

G1 Y3 E0	G1 Y3 E0	G1 Y3 E0
G1 X15 E1.6	G1 X15 E1.6	G1 X15 E1.6
G1 Y1.5 E0	G1 Y1.5 E0	G1 Y1.5 E0
G1 X0 E1.8	G1 X0 E1.8	G1 X0 E1.8
G1 Y0 E0	G1 Y0 E0	G1 Y0 E0
G0 Z0.48 E0	G0 Z0.48 E0	G0 Z0.48 E0
;LAYER 7	;LAYER 7	;LAYER 7
G1 X15 E1	G1 F200 X15 E1	G1 X15 E1
G1 Y15 E1.2	G1 Y15 E1.2	G1 Y15 E1.2
G1 X0 E1.3	G1 X0 E1.3	G1 X0 E1.3
G1 Y0 E1.4	G1 Y0 E1.4	G1 Y0 E1.4
G1 X1.5 E0	G1 F300 X1.5 E0	G1 X1.5 E0
G1 Y15 E1.6	G1 Y15 E1.6	G1 Y15 E1.6
G1 X3 E0	G1 X3 E0	G1 X3 E0
G1 Y0 E1.8	G1 Y0 E1.8	G1 Y0 E1.8
G1 X4.5 E0	G1 X4.5 E0	G1 X4.5 E0
G1 Y15 E1.9	G1 Y15 E1.9	G1 Y15 E1.9
G1 X6 E0	G1 X6 E0	G1 X6 E0
G1 Y0 E1.97	G1 Y0 E1.97	G1 Y0 E1.97
G1 X7.5 E0	G1 X7.5 E0	G1 X7.5 E0
G1 Y15 E1.2	G1 Y15 E1.2	G1 Y15 E1.2
G1 X9 E0	G1 X9 E0	G1 X9 E0
G1 Y0 E1.4	G1 Y0 E1.4	G1 Y0 E1.4
G1 X10.5 E0	G1 X10.5 E0	G1 X10.5 E0
G1 Y15 E1.6	G1 Y15 E1.6	G1 Y15 E1.6
G1 X12 E0	G1 X12 E0	G1 X12 E0
G1 Y0 E1.8	G1 Y0 E1.8	G1 Y0 E1.8
G1 X13.5 E0	G1 X13.5 E0	G1 X13.5 E0
G1 Y15 E1.9	G1 Y15 E1.9	G1 Y15 E1.9
G1 X15 Y15 E0	G1 X15 Y15 E0	G1 X15 Y15 E0
G1 Y13.5 E1.91	G1 Y13.5 E1.91	G1 Y13.5 E1.91
G1 X0 E1.92	G1 X0 E1.92	G1 X0 E1.92
G1 Y12 E0	G1 Y12 E0	G1 Y12 E0
G1 X15 E1.95	G1 X15 E1.95	G1 X15 E1.95
G1 Y10.5 E0	G1 Y10.5 E0	G1 Y10.5 E0
G1 X0 E1	G1 X0 E1	G1 X0 E1
G1 Y9 E0	G1 Y9 E0	G1 Y9 E0
G1 X15 E1.3	G1 X15 E1.3	G1 X15 E1.3
G1 Y7.5 E0	G1 Y7.5 E0	G1 Y7.5 E0
G1 X0 E1.4	G1 X0 E1.4	G1 X0 E1.4
G1 Y6 E0	G1 Y6 E0	G1 Y6 E0
G1 X15 E1	G1 X15 E1	G1 X15 E1
G1 Y4.5 E0	G1 Y4.5 E0	G1 Y4.5 E0
G1 X0 E1	G1 X0 E1	G1 X0 E1
G1 Y3 E0	G1 Y3 E0	G1 Y3 E0
G1 X15 E1.6	G1 X15 E1.6	G1 X15 E1.6

G1 Y1.5 E0	G1 Y1.5 E0	G1 Y1.5 E0
G1 X0 E1.8	G1 X0 E1.8	G1 X0 E1.8
G1 Y0 E0	G1 Y0 E0	G1 Y0 E0
G0 Z0.55 E0	G0 Z0.55 E0	G0 Z0.55 E0
;LAYER 8	;LAYER 8	;LAYER 8
G1 X15 E1	G1 F200 X15 E1	G1 X15 E1
G1 Y15 E1.2	G1 Y15 E1.2	G1 Y15 E1.2
G1 X0 E1.3	G1 X0 E1.3	G1 X0 E1.3
G1 Y0 E1.4	G1 Y0 E1.4	G1 Y0 E1.4
G1 X1.5 E0	G1 F300 X1.5 E0	G1 X1.5 E0
G1 Y15 E1.6	G1 Y15 E1.6	G1 Y15 E1.6
G1 X3 E0	G1 X3 E0	G1 X3 E0
G1 Y0 E1.8	G1 Y0 E1.8	G1 Y0 E1.8
G1 X4.5 E0	G1 X4.5 E0	G1 X4.5 E0
G1 Y15 E1.9	G1 Y15 E1.9	G1 Y15 E1.9
G1 X6 E0	G1 X6 E0	G1 X6 E0
G1 Y0 E1.97	G1 Y0 E1.97	G1 Y0 E1.97
G1 X7.5 E0	G1 X7.5 E0	G1 X7.5 E0
G1 Y15 E1.2	G1 Y15 E1.2	G1 Y15 E1.2
G1 X9 E0	G1 X9 E0	G1 X9 E0
G1 Y0 E1.4	G1 Y0 E1.4	G1 Y0 E1.4
G1 X10.5 E0	G1 X10.5 E0	G1 X10.5 E0
G1 Y15 E1.6	G1 Y15 E1.6	G1 Y15 E1.6
G1 X12 E0	G1 X12 E0	G1 X12 E0
G1 Y0 E1.8	G1 Y0 E1.8	G1 Y0 E1.8
G1 X13.5 E0	G1 X13.5 E0	G1 X13.5 E0
G1 Y15 E1.9	G1 Y15 E1.9	G1 Y15 E1.9
G1 X15 Y15 E0	G1 X15 Y15 E0	G1 X15 Y15 E0
G1 Y13.5 E1.91	G1 Y13.5 E1.91	G1 Y13.5 E1.91
G1 X0 E1.92	G1 X0 E1.92	G1 X0 E1.92
G1 Y12 E0	G1 Y12 E0	G1 Y12 E0
G1 X15 E1.95	G1 X15 E1.95	G1 X15 E1.95
G1 Y10.5 E0	G1 Y10.5 E0	G1 Y10.5 E0
G1 X0 E1	G1 X0 E1	G1 X0 E1
G1 Y9 E0	G1 Y9 E0	G1 Y9 E0
G1 X15 E1.3	G1 X15 E1.3	G1 X15 E1.3
G1 Y7.5 E0	G1 Y7.5 E0	G1 Y7.5 E0
G1 X0 E1.4	G1 X0 E1.4	G1 X0 E1.4
G1 Y6 E0	G1 Y6 E0	G1 Y6 E0
G1 X15 E1	G1 X15 E1	G1 X15 E1
G1 Y4.5 E0	G1 Y4.5 E0	G1 Y4.5 E0
G1 X0 E1	G1 X0 E1	G1 X0 E1
G1 Y3 E0	G1 Y3 E0	G1 Y3 E0
G1 X15 E1.6	G1 X15 E1.6	G1 X15 E1.6
G1 Y1.5 E0	G1 Y1.5 E0	G1 Y1.5 E0
G1 X0 E1.8	G1 X0 E1.8	G1 X0 E1.8

G1 Y0 E0	G1 Y0 E0	G1 Y0 E0
G0 Z0.63 E0	G0 Z0.63 E0	G0 Z0.63 E0
;LAYER 9	;LAYER 9	;LAYER 9
G1 X15 E1	G1 F200 X15 E1	G1 X15 E1
G1 Y15 E1.2	G1 Y15 E1.2	G1 Y15 E1.2
G1 X0 E1.3	G1 X0 E1.3	G1 X0 E1.3
G1 Y0 E1.4	G1 Y0 E1.4	G1 Y0 E1.4
G1 X1.5 E0	G1 F300 X1.5 E0	G1 X1.5 E0
G1 Y15 E1.6	G1 Y15 E1.6	G1 Y15 E1.6
G1 X3 E0	G1 X3 E0	G1 X3 E0
G1 Y0 E1.8	G1 Y0 E1.8	G1 Y0 E1.8
G1 X4.5 E0	G1 X4.5 E0	G1 X4.5 E0
G1 Y15 E1.9	G1 Y15 E1.9	G1 Y15 E1.9
G1 X6 E0	G1 X6 E0	G1 X6 E0
G1 Y0 E1.97	G1 Y0 E1.97	G1 Y0 E1.97
G1 X7.5 E0	G1 X7.5 E0	G1 X7.5 E0
G1 Y15 E1.2	G1 Y15 E1.2	G1 Y15 E1.2
G1 X9 E0	G1 X9 E0	G1 X9 E0
G1 Y0 E1.4	G1 Y0 E1.4	G1 Y0 E1.4
G1 X10.5 E0	G1 X10.5 E0	G1 X10.5 E0
G1 Y15 E1.6	G1 Y15 E1.6	G1 Y15 E1.6
G1 X12 E0	G1 X12 E0	G1 X12 E0
G1 Y0 E1.8	G1 Y0 E1.8	G1 Y0 E1.8
G1 X13.5 E0	G1 X13.5 E0	G1 X13.5 E0
G1 Y15 E1.9	G1 Y15 E1.9	G1 Y15 E1.9
G1 X15 Y15 E0	G1 X15 Y15 E0	G1 X15 Y15 E0
G1 Y13.5 E1.91	G1 Y13.5 E1.91	G1 Y13.5 E1.91
G1 X0 E1.92	G1 X0 E1.92	G1 X0 E1.92
G1 Y12 E0	G1 Y12 E0	G1 Y12 E0
G1 X15 E1.95	G1 X15 E1.95	G1 X15 E1.95
G1 Y10.5 E0	G1 Y10.5 E0	G1 Y10.5 E0
G1 X0 E1	G1 X0 E1	G1 X0 E1
G1 Y9 E0	G1 Y9 E0	G1 Y9 E0
G1 X15 E1.3	G1 X15 E1.3	G1 X15 E1.3
G1 Y7.5 E0	G1 Y7.5 E0	G1 Y7.5 E0
G1 X0 E1.4	G1 X0 E1.4	G1 X0 E1.4
G1 Y6 E0	G1 Y6 E0	G1 Y6 E0
G1 X15 E1	G1 X15 E1	G1 X15 E1
G1 Y4.5 E0	G1 Y4.5 E0	G1 Y4.5 E0
G1 X0 E1	G1 X0 E1	G1 X0 E1
G1 Y3 E0	G1 Y3 E0	G1 Y3 E0
G1 X15 E1.6	G1 X15 E1.6	G1 X15 E1.6
G1 Y1.5 E0	G1 Y1.5 E0	G1 Y1.5 E0
G1 X0 E1.8	G1 X0 E1.8	G1 X0 E1.8
G1 Y0 E0	G1 Y0 E0	G1 Y0 E0
G0 Z0.72 E0	G0 Z0.72 E0	G0 Z0.72 E0

;LAYER 10	;LAYER 10	;LAYER 10
G1 X15 E1	G1 F200 X15 E1	G1 X15 E1
G1 Y15 E1.2	G1 Y15 E1.2	G1 Y15 E1.2
G1 X0 E1.3	G1 X0 E1.3	G1 X0 E1.3
G1 Y0 E1.4	G1 Y0 E1.4	G1 Y0 E1.4
G1 X1.5 E0	G1 F300 X1.5 E0	G1 X1.5 E0
G1 Y15 E1.6	G1 Y15 E1.6	G1 Y15 E1.6
G1 X3 E0	G1 X3 E0	G1 X3 E0
G1 Y0 E1.8	G1 Y0 E1.8	G1 Y0 E1.8
G1 X4.5 E0	G1 X4.5 E0	G1 X4.5 E0
G1 Y15 E1.9	G1 Y15 E1.9	G1 Y15 E1.9
G1 X6 E0	G1 X6 E0	G1 X6 E0
G1 Y0 E1.97	G1 Y0 E1.97	G1 Y0 E1.97
G1 X7.5 E0	G1 X7.5 E0	G1 X7.5 E0
G1 Y15 E1.2	G1 Y15 E1.2	G1 Y15 E1.2
G1 X9 E0	G1 X9 E0	G1 X9 E0
G1 Y0 E1.4	G1 Y0 E1.4	G1 Y0 E1.4
G1 X10.5 E0	G1 X10.5 E0	G1 X10.5 E0
G1 Y15 E1.6	G1 Y15 E1.6	G1 Y15 E1.6
G1 X12 E0	G1 X12 E0	G1 X12 E0
G1 Y0 E1.8	G1 Y0 E1.8	G1 Y0 E1.8
G1 X13.5 E0	G1 X13.5 E0	G1 X13.5 E0
G1 Y15 E1.9	G1 Y15 E1.9	G1 Y15 E1.9
G1 X15 Y15 E0	G1 X15 Y15 E0	G1 X15 Y15 E0
G1 Y13.5 E1.91	G1 Y13.5 E1.91	G1 Y13.5 E1.91
G1 X0 E1.92	G1 X0 E1.92	G1 X0 E1.92
G1 Y12 E0	G1 Y12 E0	G1 Y12 E0
G1 X15 E1.95	G1 X15 E1.95	G1 X15 E1.95
G1 Y10.5 E0	G1 Y10.5 E0	G1 Y10.5 E0
G1 X0 E1	G1 X0 E1	G1 X0 E1
G1 Y9 E0	G1 Y9 E0	G1 Y9 E0
G1 X15 E1.3	G1 X15 E1.3	G1 X15 E1.3
G1 Y7.5 E0	G1 Y7.5 E0	G1 Y7.5 E0
G1 X0 E1.4	G1 X0 E1.4	G1 X0 E1.4
G1 Y6 E0	G1 Y6 E0	G1 Y6 E0
G1 X15 E1	G1 X15 E1	G1 X15 E1
G1 Y4.5 E0	G1 Y4.5 E0	G1 Y4.5 E0
G1 X0 E1	G1 X0 E1	G1 X0 E1
G1 Y3 E0	G1 Y3 E0	G1 Y3 E0
G1 X15 E1.6	G1 X15 E1.6	G1 X15 E1.6
G1 Y1.5 E0	G1 Y1.5 E0	G1 Y1.5 E0
G1 X0 E1.8	G1 X0 E1.8	G1 X0 E1.8
G1 Y0 E0	G1 Y0 E0	G1 Y0 E0
G0 Z0.8 E0	G0 Z0.8 E0	G0 Z0.8 E0
;LAYER 11	;LAYER 11	;LAYER 11
G1 X15 E1	G1 F200 X15 E1	G1 X15 E1

G1 Y15 E1.2	G1 Y15 E1.2	G1 Y15 E1.2
G1 X0 E1.3	G1 X0 E1.3	G1 X0 E1.3
G1 Y0 E1.4	G1 Y0 E1.4	G1 Y0 E1.4
G1 X1.5 E0	G1 F300 X1.5 E0	G1 X1.5 E0
G1 Y15 E1.6	G1 Y15 E1.6	G1 Y15 E1.6
G1 X3 E0	G1 X3 E0	G1 X3 E0
G1 Y0 E1.8	G1 Y0 E1.8	G1 Y0 E1.8
G1 X4.5 E0	G1 X4.5 E0	G1 X4.5 E0
G1 Y15 E1.9	G1 Y15 E1.9	G1 Y15 E1.9
G1 X6 E0	G1 X6 E0	G1 X6 E0
G1 Y0 E1.97	G1 Y0 E1.97	G1 Y0 E1.97
G1 X7.5 E0	G1 X7.5 E0	G1 X7.5 E0
G1 Y15 E1.2	G1 Y15 E1.2	G1 Y15 E1.2
G1 X9 E0	G1 X9 E0	G1 X9 E0
G1 Y0 E1.4	G1 Y0 E1.4	G1 Y0 E1.4
G1 X10.5 E0	G1 X10.5 E0	G1 X10.5 E0
G1 Y15 E1.6	G1 Y15 E1.6	G1 Y15 E1.6
G1 X12 E0	G1 X12 E0	G1 X12 E0
G1 Y0 E1.8	G1 Y0 E1.8	G1 Y0 E1.8
G1 X13.5 E0	G1 X13.5 E0	G1 X13.5 E0
G1 Y15 E1.9	G1 Y15 E1.9	G1 Y15 E1.9
G1 X15 Y15 E0	G1 X15 Y15 E0	G1 X15 Y15 E0
G1 Y13.5 E1.91	G1 Y13.5 E1.91	G1 Y13.5 E1.91
G1 X0 E1.92	G1 X0 E1.92	G1 X0 E1.92
G1 Y12 E0	G1 Y12 E0	G1 Y12 E0
G1 X15 E1.95	G1 X15 E1.95	G1 X15 E1.95
G1 Y10.5 E0	G1 Y10.5 E0	G1 Y10.5 E0
G1 X0 E1	G1 X0 E1	G1 X0 E1
G1 Y9 E0	G1 Y9 E0	G1 Y9 E0
G1 X15 E1.3	G1 X15 E1.3	G1 X15 E1.3
G1 Y7.5 E0	G1 Y7.5 E0	G1 Y7.5 E0
G1 X0 E1.4	G1 X0 E1.4	G1 X0 E1.4
G1 Y6 E0	G1 Y6 E0	G1 Y6 E0
G1 X15 E1	G1 X15 E1	G1 X15 E1
G1 Y4.5 E0	G1 Y4.5 E0	G1 Y4.5 E0
G1 X0 E1	G1 X0 E1	G1 X0 E1
G1 Y3 E0	G1 Y3 E0	G1 Y3 E0
G1 X15 E1.6	G1 X15 E1.6	G1 X15 E1.6
G1 Y1.5 E0	G1 Y1.5 E0	G1 Y1.5 E0
G1 X0 E1.8	G1 X0 E1.8	G1 X0 E1.8
G1 Y0 E0	G1 Y0 E0	G1 Y0 E0
G0 Z0.87 E0	G0 Z0.87 E0	G0 Z0.87 E0
;LAYER 12	;LAYER 12	;LAYER 12
G1 X15 E1	G1 F200 X15 E1	G1 X15 E1
G1 Y15 E1.2	G1 Y15 E1.2	G1 Y15 E1.2
G1 X0 E1.3	G1 X0 E1.3	G1 X0 E1.3

G1 Y0 E1.4	G1 Y0 E1.4	G1 Y0 E1.4
G1 X1.5 E0	G1 F300 X1.5 E0	G1 X1.5 E0
G1 Y15 E1.6	G1 Y15 E1.6	G1 Y15 E1.6
G1 X3 E0	G1 X3 E0	G1 X3 E0
G1 Y0 E1.8	G1 Y0 E1.8	G1 Y0 E1.8
G1 X4.5 E0	G1 X4.5 E0	G1 X4.5 E0
G1 Y15 E1.9	G1 Y15 E1.9	G1 Y15 E1.9
G1 X6 E0	G1 X6 E0	G1 X6 E0
G1 Y0 E1.97	G1 Y0 E1.97	G1 Y0 E1.97
G1 X7.5 E0	G1 X7.5 E0	G1 X7.5 E0
G1 Y15 E1.2	G1 Y15 E1.2	G1 Y15 E1.2
G1 X9 E0	G1 X9 E0	G1 X9 E0
G1 Y0 E1.4	G1 Y0 E1.4	G1 Y0 E1.4
G1 X10.5 E0	G1 X10.5 E0	G1 X10.5 E0
G1 Y15 E1.6	G1 Y15 E1.6	G1 Y15 E1.6
G1 X12 E0	G1 X12 E0	G1 X12 E0
G1 Y0 E1.8	G1 Y0 E1.8	G1 Y0 E1.8
G1 X13.5 E0	G1 X13.5 E0	G1 X13.5 E0
G1 Y15 E1.9	G1 Y15 E1.9	G1 Y15 E1.9
G1 X15 Y15 E0	G1 X15 Y15 E0	G1 X15 Y15 E0
G1 Y13.5 E1.91	G1 Y13.5 E1.91	G1 Y13.5 E1.91
G1 X0 E1.92	G1 X0 E1.92	G1 X0 E1.92
G1 Y12 E0	G1 Y12 E0	G1 Y12 E0
G1 X15 E1.95	G1 X15 E1.95	G1 X15 E1.95
G1 Y10.5 E0	G1 Y10.5 E0	G1 Y10.5 E0
G1 X0 E1	G1 X0 E1	G1 X0 E1
G1 Y9 E0	G1 Y9 E0	G1 Y9 E0
G1 X15 E1.3	G1 X15 E1.3	G1 X15 E1.3
G1 Y7.5 E0	G1 Y7.5 E0	G1 Y7.5 E0
G1 X0 E1.4	G1 X0 E1.4	G1 X0 E1.4
G1 Y6 E0	G1 Y6 E0	G1 Y6 E0
G1 X15 E1	G1 X15 E1	G1 X15 E1
G1 Y4.5 E0	G1 Y4.5 E0	G1 Y4.5 E0
G1 X0 E1	G1 X0 E1	G1 X0 E1
G1 Y3 E0	G1 Y3 E0	G1 Y3 E0
G1 X15 E1.6	G1 X15 E1.6	G1 X15 E1.6
G1 Y1.5 E0	G1 Y1.5 E0	G1 Y1.5 E0
G1 X0 E1.8	G1 X0 E1.8	G1 X0 E1.8
G1 Y0 E0	G1 Y0 E0	G1 Y0 E0
G0 Z0.93 E0	G0 Z0.93 E0	G0 Z0.93 E0
;LAYER 13	;LAYER 13	;LAYER 13
G1 X15 E1	G1 F200 X15 E1	G1 X15 E1
G1 Y15 E1.2	G1 Y15 E1.2	G1 Y15 E1.2
G1 X0 E1.3	G1 X0 E1.3	G1 X0 E1.3
G1 Y0 E1.4	G1 Y0 E1.4	G1 Y0 E1.4
G1 X1.5 E0	G1 F300 X1.5 E0	G1 X1.5 E0

G1 Y15 E1.6	G1 Y15 E1.6	G1 Y15 E1.6
G1 X3 E0	G1 X3 E0	G1 X3 E0
G1 Y0 E1.8	G1 Y0 E1.8	G1 Y0 E1.8
G1 X4.5 E0	G1 X4.5 E0	G1 X4.5 E0
G1 Y15 E1.9	G1 Y15 E1.9	G1 Y15 E1.9
G1 X6 E0	G1 X6 E0	G1 X6 E0
G1 Y0 E1.97	G1 Y0 E1.97	G1 Y0 E1.97
G1 X7.5 E0	G1 X7.5 E0	G1 X7.5 E0
G1 Y15 E1.2	G1 Y15 E1.2	G1 Y15 E1.2
G1 X9 E0	G1 X9 E0	G1 X9 E0
G1 Y0 E1.4	G1 Y0 E1.4	G1 Y0 E1.4
G1 X10.5 E0	G1 X10.5 E0	G1 X10.5 E0
G1 Y15 E1.6	G1 Y15 E1.6	G1 Y15 E1.6
G1 X12 E0	G1 X12 E0	G1 X12 E0
G1 Y0 E1.8	G1 Y0 E1.8	G1 Y0 E1.8
G1 X13.5 E0	G1 X13.5 E0	G1 X13.5 E0
G1 Y15 E1.9	G1 Y15 E1.9	G1 Y15 E1.9
G1 X15 Y15 E0	G1 X15 Y15 E0	G1 X15 Y15 E0
G1 Y13.5 E1.91	G1 Y13.5 E1.91	G1 Y13.5 E1.91
G1 X0 E1.92	G1 X0 E1.92	G1 X0 E1.92
G1 Y12 E0	G1 Y12 E0	G1 Y12 E0
G1 X15 E1.95	G1 X15 E1.95	G1 X15 E1.95
G1 Y10.5 E0	G1 Y10.5 E0	G1 Y10.5 E0
G1 X0 E1	G1 X0 E1	G1 X0 E1
G1 Y9 E0	G1 Y9 E0	G1 Y9 E0
G1 X15 E1.3	G1 X15 E1.3	G1 X15 E1.3
G1 Y7.5 E0	G1 Y7.5 E0	G1 Y7.5 E0
G1 X0 E1.4	G1 X0 E1.4	G1 X0 E1.4
G1 Y6 E0	G1 Y6 E0	G1 Y6 E0
G1 X15 E1	G1 X15 E1	G1 X15 E1
G1 Y4.5 E0	G1 Y4.5 E0	G1 Y4.5 E0
G1 X0 E1	G1 X0 E1	G1 X0 E1
G1 Y3 E0	G1 Y3 E0	G1 Y3 E0
G1 X15 E1.6	G1 X15 E1.6	G1 X15 E1.6
G1 Y1.5 E0	G1 Y1.5 E0	G1 Y1.5 E0
G1 X0 E1.8	G1 X0 E1.8	G1 X0 E1.8
G1 Y0 E0	G1 Y0 E0	G1 Y0 E0
G0 Z1 E0	G0 Z1 E0	G0 Z1 E0
;LAYER 14	;LAYER 14	;LAYER 14
G1 X15 E1	G1 F200 X15 E1	G1 X15 E1
G1 Y15 E1.2	G1 Y15 E1.2	G1 Y15 E1.2
G1 X0 E1.3	G1 X0 E1.3	G1 X0 E1.3
G1 Y0 E1.4	G1 Y0 E1.4	G1 Y0 E1.4
G1 X1.5 E0	G1 F300 X1.5 E0	G1 X1.5 E0
G1 Y15 E1.6	G1 Y15 E1.6	G1 Y15 E1.6
G1 X3 E0	G1 X3 E0	G1 X3 E0

G1 Y0 E1.8	G1 Y0 E1.8	G1 Y0 E1.8
G1 X4.5 E0	G1 X4.5 E0	G1 X4.5 E0
G1 Y15 E1.9	G1 Y15 E1.9	G1 Y15 E1.9
G1 X6 E0	G1 X6 E0	G1 X6 E0
G1 Y0 E1.97	G1 Y0 E1.97	G1 Y0 E1.97
G1 X7.5 E0	G1 X7.5 E0	G1 X7.5 E0
G1 Y15 E1.2	G1 Y15 E1.2	G1 Y15 E1.2
G1 X9 E0	G1 X9 E0	G1 X9 E0
G1 Y0 E1.4	G1 Y0 E1.4	G1 Y0 E1.4
G1 X10.5 E0	G1 X10.5 E0	G1 X10.5 E0
G1 Y15 E1.6	G1 Y15 E1.6	G1 Y15 E1.6
G1 X12 E0	G1 X12 E0	G1 X12 E0
G1 Y0 E1.8	G1 Y0 E1.8	G1 Y0 E1.8
G1 X13.5 E0	G1 X13.5 E0	G1 X13.5 E0
G1 Y15 E1.9	G1 Y15 E1.9	G1 Y15 E1.9
G1 X15 Y15 E0	G1 X15 Y15 E0	G1 X15 Y15 E0
G1 Y13.5 E1.91	G1 Y13.5 E1.91	G1 Y13.5 E1.91
G1 X0 E1.92	G1 X0 E1.92	G1 X0 E1.92
G1 Y12 E0	G1 Y12 E0	G1 Y12 E0
G1 X15 E1.95	G1 X15 E1.95	G1 X15 E1.95
G1 Y10.5 E0	G1 Y10.5 E0	G1 Y10.5 E0
G1 X0 E1	G1 X0 E1	G1 X0 E1
G1 Y9 E0	G1 Y9 E0	G1 Y9 E0
G1 X15 E1.3	G1 X15 E1.3	G1 X15 E1.3
G1 Y7.5 E0	G1 Y7.5 E0	G1 Y7.5 E0
G1 X0 E1.4	G1 X0 E1.4	G1 X0 E1.4
G1 Y6 E0	G1 Y6 E0	G1 Y6 E0
G1 X15 E1	G1 X15 E1	G1 X15 E1
G1 Y4.5 E0	G1 Y4.5 E0	G1 Y4.5 E0
G1 X0 E1	G1 X0 E1	G1 X0 E1
G1 Y3 E0	G1 Y3 E0	G1 Y3 E0
G1 X15 E1.6	G1 X15 E1.6	G1 X15 E1.6
G1 Y1.5 E0	G1 Y1.5 E0	G1 Y1.5 E0
G1 X0 E1.8	G1 X0 E1.8	G1 X0 E1.8
G1 Y0 E0	G1 Y0 E0	G1 Y0 E0
;LAYER 15	;LAYER 15	;LAYER 15
G92 E0	G92 E0	G92 E0
; Filament-specific end gcode	; Filament-specific end gcode	; Filament-specific end gcode
;END gcode for filament	;END gcode for filament	;END gcode for filament

References

[1] P. Guardia, A. Riedinger, S. Nitti, G. Pugliese, S. Marras, A. Genovese, M.E. Materia, C. Lefevre, L. Manna, T. Pellegrino, One pot synthesis of monodisperse water soluble iron oxide nanocrystals with high values of the specific absorption rate, Journal of Materials Chemistry B 2(28) (2014) 4426-4434.